Monthly Notices
of the
ROYAL ASTRONOMICAL SOCIETY

MNRAS **467,** 1569–1585 (2017)
Advance Access publication 2017 January 22

doi:10.1093/mnras/stx196

Real- and redshift-space halo clustering in $f(R)$ cosmologies

Pablo Arnalte-Mur,[1,2,3]★ Wojciech A. Hellwing[4,2,5] and Peder Norberg[2,6]

[1]*Observatori Astronòmic de la Universitat de València, C/Catedràtic José Beltrán, 2, E-46980 Paterna, Spain*
[2]*Institute for Computational Cosmology, Department of Physics, Durham University, South Road, Durham DH1 3LE, UK*
[3]*Departament d'Astronomia i Astrofísica, Universitat de València, E-46100 Burjassot, Spain*
[4]*Institute of Cosmology and Gravitation, University of Portsmouth, Portsmouth PO1 3FX, UK*
[5]*Janusz Gil Institute of Astronomy, University of Zielona Góra, ul. Szafrana 2, PL-65-516 Zielona Góra, Poland*
[6]*Centre for Extragalactic Astronomy, Department of Physics, Durham University, South Road, Durham DH1 3LE, UK*

Accepted 2017 January 19. Received 2017 January 18; in original form 2016 December 7

ABSTRACT

We present two-point correlation function statistics of the mass and the haloes in the chameleon $f(R)$ modified gravity scenario using a series of large-volume N-body simulations. Three distinct variations of $f(R)$ are considered (F4, F5 and F6) and compared to a fiducial Λ cold dark matter (ΛCDM) model in the redshift range $z \in [0, 1]$. We find that the matter clustering is indistinguishable for all models except for F4, which shows a significantly steeper slope. The ratio of the redshift- to real-space correlation function at scales $>20\,h^{-1}$ Mpc agrees with the linear General Relativity (GR) Kaiser formula for the viable $f(R)$ models considered. We consider three halo populations characterized by spatial abundances comparable to that of luminous red galaxies and galaxy clusters. The redshift-space halo correlation functions of F4 and F5 deviate significantly from ΛCDM at intermediate and high redshift, as the $f(R)$ halo bias is smaller than or equal to that of the ΛCDM case. Finally, we introduce a new model-independent clustering statistic to distinguish $f(R)$ from GR: the relative halo clustering ratio – $\mathcal{R}$. The sampling required to adequately reduce the scatter in $\mathcal{R}$ will be available with the advent of the next-generation galaxy redshift surveys. This will foster a prospective avenue to obtain largely model-independent cosmological constraints on this class of modified gravity models.

Key words: gravitation – methods: data analysis – cosmology: theory – dark matter – large-scale structure of Universe.

1 INTRODUCTION

The hot relativistic big-bang Λ cold dark matter (ΛCDM) cosmology is a very successful standard model of cosmology. It passes a tremendous amount of observational tests, from properties of the cosmic microwave background (e.g. Hinshaw et al. 2013), large-scale clustering of galaxies (e.g. Cole et al. 2005; Eisenstein et al. 2005; Zehavi et al. 2011; Alam et al. 2016), weak and strong lensing (e.g. Bartelmann & Schneider 2001; Schrabback et al. 2010; Suyu et al. 2013) to properties of galaxy clusters, galaxies and their satellites in the nearby Universe (e.g. Mandelbaum et al. 2006; Allen, Evrard & Mantz 2011; Wojtak, Hansen & Hjorth 2011; Guo et al. 2015; Umetsu et al. 2016). The minimum set of parameters describing this simple scenario has now been established to a remarkable precision (Planck Collaboration XIII 2016). Despite its undeniable success, the standard ΛCDM model suffers from serious theoretical problems. The model explains the observed late-time acceleration of the Universe (Riess et al. 1998; Perlmutter et al. 1999) by attributing it to a very low positive value of Einstein's cosmological constant, Λ. One of the main shortcomings of this approach comprises the fact that the only known possible physical explanation of the non-zero Λ is the zero-point energy of vacuum quantum fluctuations. However, quantum theory predicts a natural value for Λ that is many orders of magnitude larger than the actual value that is compatible with observations (for an excellent discussion, see e.g. Carroll 2001, and references therein). The unavoidable conclusion is that one of the fundamental ingredients of the equations describing the evolution of the cosmological background is lacking a clear physical interpretation. In addition, General Relativity (GR), as any working physical theory, itself needs to be continuously tested on all scales and regimes accessible through experiments and observations (Will 2014).

The conceptual problems of ΛCDM have motivated a number of theoretical modifications to the standard model, which can produce the observed late-time acceleration of the Universe by means of different physical mechanisms. The rich literature on the subject can be divided broadly into two distinct categories. In the first, it

★ E-mail: pablo.arnalte@uv.es

is postulated that the acceleration is produced by a dynamically evolving background scalar field (for a solid review of the subject, see Copeland, Sami & Tsujikawa 2006). These models, usually invoking a minimally coupled scalar field, are collectively dubbed as dark energy. The second category consists of theories where the accelerated expansion is a manifestation of the modifications to the Einstein–Hilbert action integral. That is, they implement modifications to the theory of GR, an otherwise fundamental building block of modern cosmology (Brax et al. 2008; Clifton et al. 2012; Koyama 2016). The latter class of models are the so-called modified gravity (MOG) models. Here the late-time acceleration is fuelled by extra terms appearing in the cosmic Lagrangian and that act as an 'effective Lambda' term. Thus, in this approach, a mechanism that would set the usual cosmological constant to exactly zero is needed. Since such a mechanism has not yet been discovered, this approach should not be regarded as an attempt to construct a new fundamental theory of gravity, but rather an effort to probe the rich phenomenology of infrared modifications to GR, with non-trivial effects on cosmological scales. MOG models, in principle, can be constructed in many different ways. In the recent years, one of the broadly investigated models, which falls into the MOG category, is the so-called $f(R)$ gravity theory. In this case, the accelerated expansion is produced by an extra term replacing Λ in the action integral. This term consists of a non-linear function f taking as an argument the curvature scalar R (Navarro & Van Acoleyen 2007; de Felice & Tsujikawa 2010; Sotiriou & Faraoni 2010). This class of models exhibit rich and interesting new physics. In addition to producing late-time acceleration, they admit for a non-negligible fifth force acting on small and intermediate cosmological scales (i.e. much smaller than the horizon, $\ll cH_0^{-1}$). This non-trivial and intrinsically non-linear fifth force can manifest itself in deviations of the large- and small-scale clustering of galaxies and matter from the standard GR picture. In other words: in $f(R)$ gravity one can have a universe exhibiting GR, or ΛCDM-like, expansion history but admitting, at the same time, a different history of growth of structures (Faulkner et al. 2007; Brax et al. 2008; Oyaizu, Lima & Hu 2008; Li et al. 2013).

Any potentially successful MOG theory is required to not only predict a global expansion history compatible with observations but also needs to pass stringent local tests of gravity. The latter come from observed orbital dynamics in the Solar system (e.g. Chiba, Smith & Erickcek 2007; Hu & Sawicki 2007; Berry & Gair 2011), pulsar timing (Brax, Davis & Sakstein 2014) and as of recently the physics of gravitational waves emitted during black hole mergers (Raveri et al. 2015; Abbott et al. 2016). See also Berti et al. (2015) for a discussion of other astrophysical tests of MOG. In the most general class of $f(R)$ theories, the fifth force can freely propagate whenever there is a gradient of the $f(R)$ scalar field (also called the *scalaron*). Thus, if this model wants to stay compatible with the local gravity tests, it needs to implement a mechanism for suppressing the fifth force in high-density regions, like our Solar system or neutron star binaries. In $f(R)$ theories, this is accomplished by a convenient choice of the $f(R)$ function that gives rise to the so-called *chameleon mechanism* (Khoury & Weltman 2004; Brax et al. 2008). The chameleon mechanism makes the scalaron very massive in spatial regions of high local curvature (density); this leads to an effective suppression of any fifth-force propagation. Contrastingly, in regions with a low local density, the field is light and admits the propagation of the scalar fifth force. The effectiveness of the chameleon suppression is moderated by the local density field. This makes this mechanism to be *intrinsically* environment dependent and thus highly non-linear in its nature. Consequently, in this scenario, one can have regions of low cosmic density (such as e.g. cosmic voids) in which the fifth force strongly affects the dynamics and clustering of galaxies, as well as regions with higher density, where the theory can effectively behave as the classical GR. As the degree of non-linearity in both matter and scalar cosmic fields increases fast during cosmic evolution, it quickly renders predictions of simple linear and weakly non-linear perturbation theory unreliable (e.g. Hellwing 2015). Because of this, the use of N-body computer simulations is essential for forecasting reliable and accurate predictions. However, the same very non-linear nature makes such simulations much more challenging and more expensive than standard GR simulations. In the recent years, there has been a significant progress in the development of MOG N-body solvers (e.g. Llinares, Knebe & Zhao 2008; Oyaizu 2008; Schmidt, Vikhlinin & Hu 2009b; Zhao, Li & Koyama 2011; Li et al. 2012a; Llinares & Mota 2013, 2014; Puchwein, Baldi & Springel 2013; Winther et al. 2015; Bose et al. 2016). As an outcome, modern codes are not only capable of running large-volume and high-resolution simulations, but also have attained the accuracy needed for the precision cosmology era of the current and forthcoming galaxy surveys, such as *Euclid* (Laureijs et al. 2011), the Dark Energy Spectroscopic Instrument (DESI) survey (Levi et al. 2013) or the Javalambre-Physics of the Accelerated Universe Astrophysical Survey (J-PAS; Benitez et al. 2014). Thanks to this, it is now possible to study the galaxy, halo and matter clustering properties of $f(R)$ gravity models with sufficient resolution.

In general, we can expect that in $f(R)$ models the modifications to GR will manifest themselves as a modified history of growth of structures, and thus will also affect the galaxy clustering and dynamics. It has been shown in the literature that indeed this class of models exhibit higher amplitude of matter power spectrum at small and intermediate scales (i.e. $\lesssim 20\,h^{-1}$ Mpc; Oyaizu et al. 2008; Gil-Marín et al. 2011; Li et al. 2013), and even on larger scales for the case of higher order clustering amplitudes (Hellwing et al. 2013). Dark matter (DM) clustering in redshift space is also characterized by stronger Finger-of-God (FOG) effects at small scales (Jackson 1972), which is accompanied by more pronounced Kaiser effect (Kaiser 1987; Hamilton 1992) at larger scales (Jennings et al. 2012). The stronger FOG, which leads to more effective small-scale power damping in redshift space, is a manifestation of dynamics enhanced by the fifth force. This effective enhancement was also shown to be predicted, as a prominent MOG 'smoking gun' feature, for the galaxy/DM halo velocity field (Hellwing et al. 2014). Other studies have shown that $f(R)$ models can lead to different predictions for density profiles and size of cosmic voids (Li, Zhao & Koyama 2012b; Cai, Padilla & Li 2015), modified stellar evolution (Sakstein 2015) or several characteristics of galaxy clusters: number counts (Schmidt et al. 2009b), X-ray or lensing radial profiles (Wilcox et al. 2016) and measured gas fractions (Li, He & Gao 2016).

All the above-mentioned effects of MOG in general should manifest themselves in observations as deviations from the GR-based predictions. However, the highly non-linear character of the galaxy formation process makes it very difficult to foster observational predictions with respect to GR/MOG differences. Highly energetic processes, such as star formation feedback and active galactic nuclei (AGN) feedback, affect the matter distribution up to scales of $20\,h^{-1}$ Mpc (e.g. van Daalen et al. 2011, 2014; Hellwing et al. 2016). It was shown that, when matter clustering is concerned, the baryonic feedback effects are degenerate with enhanced clustering predicted by pure collisionless simulations of $f(R)$ (Puchwein et al. 2013). Therefore, a good strategy aimed to find a

clean $f(R)$ signature is to look at both larger scales and at more massive haloes. Here one can expect that the baryonic effects should be relatively weaker, giving hope of reducing the baryonic–MOG effects degeneracy.

These previous works have studied the expected changes in the growth of structures in $f(R)$ models by analysing the changes in different clustering properties of the DM density field. However, in order to be able to compare the models with observational data from galaxy surveys, one needs to obtain a prediction for the clustering of galaxies. This involves studying possible differences in the biasing mechanism between ΛCDM and the $f(R)$ models. In principle, this would require the modelling of the galaxy formation process in the $f(R)$ theory. A first step in this direction is to study the clustering properties of DM haloes, as the bias of galaxies is closely related to the bias of the haloes in which they reside. Moreover, when we restrict the study to the most massive haloes and linear or quasi-linear scales, the clustering of DM haloes is a good proxy for the clustering of the corresponding central galaxies. A complementary approach was followed by He, Li & Baugh (2016) who used the sub-halo abundance matching technique to study the clustering of galaxies in the $f(R)$ model at small non-linear scales ($r \leq 6\,h^{-1}$ Mpc).

The aim of this work is therefore to characterize the clustering properties of DM haloes in a set of $f(R)$ models and compare them to the ΛCDM model. We explain how the clustering of massive haloes is affected by $f(R)$ enhanced dynamics in both real and redshift space. We also conduct our study for a range of cosmic times, aiming to find the epoch of cosmic evolution at which the relative differences between the models are strongest. Our ultimate goal is to confront the theoretical predictions with observations from galaxy redshift surveys. Hence, when selecting our samples and defining our clustering observables, we try to match what could be feasible when using real data. Following this approach, we define a new statistic that can be easily measured from observations, and that can potentially help discriminate between GR and $f(R)$ cosmologies in the real Universe.

This paper is organized as follows. In Section 2, we give a brief description of both the physical set-up of the $f(R)$ model and of the numerical simulations used in this work. The clustering statistics and the definition of the different halo samples that we use are described in Section 3. Section 4 concerns the results of our analysis, while in Section 5 we discuss potential observational clustering tests using the new clustering ratio statistic. Finally, in Section 6 we give our conclusions.

2 THE $f(R)$ GRAVITY THEORY AND SIMULATIONS

Here we briefly introduce the physical set-up and basic properties of the $f(R)$ MOG model accompanied by a description of the numerical structure formation simulations used in this work.

2.1 The $f(R)$ gravity theory

The $f(R)$ gravity (Carroll et al. 2005) is an extension of GR that has been extensively studied in the literature in the past few years. The main properties of the model are widely known; hence, we will focus here on only a very brief introduction of this theory, referring the reader for more details to the rich literature on the subject (see e.g. de Felice & Tsujikawa 2010; Sotiriou & Faraoni 2010, for detailed reviews).

The theory is obtained by substituting the Ricci scalar R in the Einstein–Hilbert action with an algebraic function $f(R)$,

$$S = \int \mathrm{d}^4x\sqrt{-g}\left\{\frac{M_{\rm Pl}^2}{2}\left[R + f(R)\right] + \mathcal{L}_{\rm m}\right\}. \quad (1)$$

Here $M_{\rm Pl}$ is the reduced Planck mass, $M_{\rm Pl}^{-2} = 8\pi G$, G is Newton's constant, g the determinant of the metric $g_{\mu\nu}$ and $\mathcal{L}_{\rm m}$ the Lagrangian density for matter and radiation fields (including photons, neutrinos, baryons and cold dark matter). By designing the functional form of $f(R)$, one can fully specify a $f(R)$ gravity model.

Varying the action, equation (1), with respect to the metric field $g_{\mu\nu}$, one obtains the modified Einstein equation

$$G_{\mu\nu} + f_R R_{\mu\nu} - g_{\mu\nu}\left[\frac{1}{2}f(R) - \Box f_R\right] - \nabla_\mu\nabla_\nu f_R = 8\pi G T^{\rm m}_{\mu\nu}, \quad (2)$$

where $G_{\mu\nu} \equiv R_{\mu\nu} - \frac{1}{2}g_{\mu\nu}R$ is the Einstein tensor, $f_R \equiv \mathrm{d}f/\mathrm{d}R$, ∇_μ is the covariant derivative compatible with $g_{\mu\nu}$, $\Box \equiv \nabla^\alpha\nabla_\alpha$ and $T^{\rm m}_{\mu\nu}$ is the energy momentum tensor of matter and radiation fields. Equation (2) is a fourth-order differential equation, but can also be considered as the standard second-order equation of GR with a new dynamical degree of freedom, f_R, the equation of motion of which can be obtained by taking the trace of equation (2)

$$\Box f_R = \frac{1}{3}\left(R - f_R R + 2f(R) + 8\pi G\rho_{\rm m}\right), \quad (3)$$

where $\rho_{\rm m}$ is the matter density. This new degree of freedom f_R is the scalaron mentioned earlier.

Our analysis here is mainly concerned with large-scale structures, which are much smaller than the Hubble scale. Since the time variation of f_R is very small in the models to be considered below, we shall work in the quasi-static limit by neglecting the time derivatives of f_R. It has been shown that by adopting this approximation, the resulting modelled dynamics of the scalar and matter fields deviates negligibly from the true dynamics (Bose, Hellwing & Li 2015). Under this limit, the f_R equation of motion, equation (3), reduces to

$$\vec{\nabla}^2 f_R = -\frac{1}{3}a^2\left[R - \bar{R} + 8\pi G\left(\rho_{\rm m} - \bar{\rho}_{\rm m}\right)\right], \quad (4)$$

where $\vec{\nabla}$ is the three-dimensional gradient operator, and the overbar takes the background ensemble average of a quantity.

Similarly, the Poisson equation, which governs the behaviour of the gravitational potential Φ, simplifies to

$$\vec{\nabla}^2\Phi = \frac{16\pi G}{3}a^2\left(\rho_{\rm m} - \bar{\rho}_{\rm m}\right) + \frac{1}{6}a^2\left[R - \bar{R}\right], \quad (5)$$

by neglecting terms involving time derivatives of Φ and f_R, and using equation (4) to eliminate $\vec{\nabla}^2 f_R$.

The above considerations foster two ways in which the scalaron field can affect cosmology: (i) the background expansion of the Universe can be modified by the new terms in equation (2) and (ii) the relationship between the gravitational potential Φ and the matter density field is modified, which can affect the matter clustering and growth of density perturbations. Clearly, when $|f_R| \ll 1$, we have $R \approx -8\pi G\rho_{\rm m}$ (see equation 4) and thus equation (5) reduces to the usual Poisson equation; when $|f_R|$ is large, we will have rather $|R - \bar{R}| \ll 8\pi G|\rho_{\rm m} - \bar{\rho}_{\rm m}|$ and then equation (5) simplifies to the standard Poisson equation, but with G rescaled by 4/3. The value 1/3 is the maximum intensification factor of gravity in $f(R)$ models, independent of the specific functional form of $f(R)$. The choice of $f(R)$, however, is crucial because it determines the scalaron dynamics and therefore when and on what scales the enhancement factor

changes from 1 to 4/3. Scales much larger than the range of the modification to Newtonian gravity mediated by the scalaron field (i.e. the Compton wavelength of f_R) are unaffected, and gravity is not enhanced there, while on small scales, depending on the environmental matter density, the 1/3 enhancement may be fully realized. This results in a scale-dependent modification of gravity and therefore a scale-dependent growth rate of structures already at the linear theory level (Koyama, Taruya & Hiramatsu 2009).

2.1.1 *The chameleon mechanism*

The gravity and Newtonian dynamics passes stringent tests coming from the Solar system observations, and so any 4/3 force enhancement factor related to $f(R)$ needs to avoid high-density regions as our Solar system. The theory achieves this by implementing the so-called chameleon screening mechanism.

The basic idea of the chameleon mechanism is the following: the modifications to Newtonian gravity can be considered as a fifth force mediated by the scalaron field f_R. Because the scalaron is massive, this extra force experiences a Yukawa-type potential. Hence, the enhanced gravity is decaying exponentially as $\exp(-mr)$, in which m is the scalaron mass, as the distance r between two test masses increases. In high matter density environments, m is very heavy and the exponential decay causes a strong suppression of the force over distance. In reality, this is equivalent to setting $|f_R| \ll 1$ in high-density regions because f_R is the potential of the fifth force, and this leads to the GR limit as we have discussed above.

Consequently, the functional form of $f(R)$ is crucial in determining whether the fifth force can be sufficiently suppressed in high-density environments. In this work, we consider the $f(R)$ Lagrangian proposed by Hu & Sawicki (2007), for which

$$f(R) = -M^2 \frac{c_1 \left(-R/M^2\right)^n}{c_2 \left(-R/M^2\right)^n + 1}, \tag{6}$$

where $M^2 \equiv 8\pi G\bar{\rho}_{\rm m0}/3 = H_0^2\Omega_{\rm M}$, with H being the Hubble expansion rate and $\Omega_{\rm M}$ the present-day fractional density of matter. Throughout the paper, a subscript 0 always denotes the present-day ($a = 1$, $z = 0$) value of a quantity. It was shown by Hu & Sawicki (2007) that $|f_{R0}| \lesssim 0.1$ is already sufficient to pass the Solar system constraints, but the exact constraint depends on the behaviour of f_R in galaxies and pulsating stars as well (Sakstein 2013, 2015). At the background level, the scalaron f_R always sits close to the minimum of the effective potential; therefore, for the smooth scalar field, we have (Brax et al. 2012)

$$-\bar{R} \approx 8\pi G\bar{\rho}_{\rm m} - 2f(\bar{R}) = 3M^2\left(a^{-3} + \frac{2c_1}{3c_2}\right). \tag{7}$$

The Hu–Sawicki model we consider is fixed by requesting that the background expansion history matches that of ΛCDM. Thus, we set

$$\frac{c_1}{c_2} = 6\frac{\Omega_\Lambda}{\Omega_{\rm M}}, \tag{8}$$

where $\Omega_{\rm M}$ and Ω_Λ are respectively the present-day fractional energy densities of the matter and dark energy. The simulation we use in this work uses *Wilkinson Microwave Anisotropy Probe* 3 cosmological background parameters (Spergel et al. 2007, see Table 1). Using $\Omega_\Lambda = 0.76$ and $\Omega_{\rm M} = 0.24$ and equation (7) gives $|\bar{R}| \approx 41M^2 \gg M^2$ at late times. Using this approximation simplifies the expression of the scalaron to the following form:

$$f_R \approx -n\frac{c_1}{c_2^2}\left(\frac{M^2}{-R}\right)^{n+1}. \tag{9}$$

Table 1. Main properties of the simulations used in this work, for more details please see Li et al. (2013) and Hellwing et al. (2013).

Models	ΛCDM, F6, F5, F4
Number of realizations	6
Box size	$L_{\rm box} = 1500\,h^{-1}$ Mpc
Number of particles	$N_{\rm p} = 1024^3$
Particle mass	$m_{\rm p} \simeq 2 \times 10^{11}\,h^{-1}\,{\rm M}_\odot$
Nyquist frequency	$k_{\rm Nyq} = 2.14\,h\,{\rm Mpc}^{-1}$
Force resolution	$\epsilon = 22.9\,h^{-1}$ kpc
Cosmological parameters:	
Total matter density	$\Omega_{\rm M} = 0.24$
Dark energy density	$\Omega_\Lambda = 0.76$
Baryonic matter density	$\Omega_{\rm b} = 0.041\,81$
Dimensionless Hubble parameter	$h = 0.73$
Tilt factor of the initial power spectrum	$n_{\rm s} = 0.958$
Power spectrum normalization	$\sigma_8 = 0.77$
BAO peak scale (linear theory)	$r_{\rm BAO} \simeq 113\,h^{-1}$ Mpc

The above considerations show that once a ΛCDM background is fixed, our chosen $f(R)$ model is completely specified by the two free parameters: n and c_1/c_2^2. Henceforth, the ratio c_1/c_2^2 is also fixed by the averaged background value of the scalaron, f_{R0}, at $z = 0$. This yields

$$\frac{c_1}{c_2^2} = -\frac{1}{n}\left[3\left(1 + 4\frac{\Omega_\Lambda}{\Omega_{\rm M}}\right)\right]^{n+1} f_{R0}. \tag{10}$$

Thus, the choice of f_{R0} and n fully specifies our model.

The particular $f(R)$ set-up we consider here has very interesting cosmological properties. At small scales in regions where the local density is high, the enhanced gravity will be suppressed and the dynamics will be Newtonian. Hence, we can expect that orbital satellites and halo close interactions will be very similar as in GR. However, in regions exhibiting low densities, such as e.g. cosmic voids, the modified dynamics should affect both halo and galaxy clustering and velocities. We specifically consider three flavours of the Hu–Sawicki $f(R)$ model with fixed $n = 1$, which differ in the present-day mean (background) scalaron value $|f_{R0}| = 10^{-4}$, 10^{-5} and 10^{-6}. We dub the models F4, F5 and F6 consequently. These three models cover the portion of the $f(R)$ parameter space that produce interesting cosmological effects and is still compatible with extragalactic observations. While F5 and F6 are so far in a broad agreement with the cosmological observations, F4 however is already in a strong tension with observations of cluster number counts (Schmidt et al. 2009b; Ferraro, Schmidt & Hu 2011; Lombriser et al. 2012; Cataneo et al. 2015) or weak lensing (Harnois-Déraps et al. 2015; Liu et al. 2016). Thus, we shall use F4 results just as an extreme example of effects induced by only weakly screened fifth force.

2.2 Cosmological $f(R)$ simulations used in this work

In this work, we use the $f(R)$ simulations introduced in Li et al. (2013). Most of the previous work however focused on DM density fields only. Here we are very much interested in clustering properties of DM haloes (and ultimately galaxies). For that reason, we have applied ROCKSTAR, a phase-space Friends-of-Friends (FOF) halo finder (Behroozi, Wechsler & Wu 2013). We kept all the haloes that contained at least 100 DM particles; hence, this sets our minimal halo mass limit to $M_{\rm min} = 2.09 \times 10^{13}\,h^{-1}\,{\rm M}_\odot$. Further on, we recompute the FOF halo mass using a proper virial mass definition. For the virial mass, we use M_{200}, i.e. the mass contained in a sphere of

radius r_{200} centred on a halo, such that the average overdensity inside the sphere is 200 times the critical closure density, $\rho_c \equiv 3H^2/8\pi G$. Our adopted mass cut left us with $\sim 10^6$ haloes at $z = 0$ for each initial condition realization. Thus, the upper limit on our spatial number density of objects is $\bar{n} = 3 \times 10^{-4}\, h^3\,\mathrm{Mpc}^{-3}$ at $z = 0$ and correspondingly smaller at higher redshifts. Our simulations use a computational domain of $1500\,h^{-1}$ Mpc size. Following the analyses by other authors of the importance of both finite-volume effects (e.g. Colombi, Bouchet & Schaeffer 1994) and sparse sampling (e.g. Szapudi & Colombi 1996), we adopt conservative limits on the minimal and maximal scales that we trust. For a minimum scale, we adopt a limit of $3 \times 2\pi k_{\mathrm{Nyq}}^{-1} \simeq 10\,h^{-1}$ Mpc, where the Nyquist frequency for the simulations is $k_{\mathrm{Nyq}} = 2.14\,h\,\mathrm{Mpc}^{-1}$. We take as the maximum scale to study $1/10 \times L_{\mathrm{box}} \simeq 150\,h^{-1}$ Mpc, as we expect larger scales to be affected by the finite-volume effects. Finally, we will focus our analysis on four snapshots taken consecutively at $z = 0$, 0.25, 0.66 and 1.0. Previous studies (Hellwing et al. 2013) have shown that for those times the differences between GR and $f(R)$ clustering are expected to be the largest. We list other details of the simulations used here in Table 1.

3 ANALYSIS OF HALO CLUSTERING IN *N*-BODY SIMULATIONS

The astronomical observations that provide the data characterizing the clustering of matter at large scales contain information only about the luminous stellar matter distribution in our Universe. Contemporary galaxy redshift catalogues contain positions of millions of galaxies, observed over large parts of the sky and over vast distances (redshifts). Ideally, one would like then to study the clustering of galaxies in various competing cosmological models. This requires however introduction of another component into a theory under investigation, namely the galaxy formation model.

Various techniques exist that allow for galaxy formation modelling, the semi-analytic models (for a review see Baugh 2006), hydrodynamical simulations (Vogelsberger et al. 2014; Schaye et al. 2015) and abundance matching (Kravtsov et al. 2004; Moster et al. 2010), to just name a few. However, all the existing techniques were developed and tested self-consistently only for the ΛCDM model. Application and extrapolation of such modelling to MOG models is neither straightforward nor simple (Fontanot et al. 2013). In addition, the existing ΛCDM galaxy formation models are still subject of intensive scrutiny (Contreras et al. 2013), as our understanding of the importance and interconnection of all the complicated baryonic feedback processes is far from being full and complete (see e.g. Fabjan et al. 2010; McCarthy et al. 2010; Schaye et al. 2010; McCarthy et al. 2011; Puchwein & Springel 2013). In addition, the strength and the environmental dependence of the additional fifth force of the $f(R)$ model impact the galaxy clustering in a way that is degenerated with strong baryonic feedback invoked by AGN and galaxy winds (Puchwein et al. 2013).

Taking into account all the difficulties mentioned above and the challenges connected with galaxy formation, we decide to follow a simpler approach. We use DM haloes and their clustering properties as proxies for galaxy clustering. Haloes are well-defined objects (both in ΛCDM and $f(R)$), and as such can be straightforwardly identified and extracted from *N*-body simulations (Knebe et al. 2011).

We expect that in $f(R)$ gravity the galaxy formation mechanism and processes involved can, in principle, take largely different character than in ΛCDM. However, if we restrict the analysis to a sample of very luminous galaxies, the situation is simpler. In this case, the fraction of satellite galaxies is very small (e.g. Zheng et al. 2009), so we can assume that most of the galaxies are located at the centres of massive DM haloes and the galaxy clustering properties will follow closely those of the host haloes. This is certainly a valid approximation if we constrain ourselves to sufficiently large scales (i.e. the two-halo term limit, $\geq 10\,h^{-1}$ Mpc). Moreover, for this type of galaxy samples, it is possible to remove the effect of the satellite galaxies from clustering measurements (Reid, Spergel & Bode 2009). Going further to the high-mass end of the mass function, DM haloes correspond to galaxy groups or clusters, which can be identified from galaxy surveys (see e.g. Koester et al. 2007; Robotham et al. 2011; Ascaso et al. 2015). In this regime, the clustering of DM haloes in different models can be directly compared to that of observed groups.

To characterize the clustering of matter and haloes (in position and redshift space) at different scales and epochs, we use a basic two-point statistic: the two-point correlation function, $\xi(r)$. This is defined as (Peebles 1980) the excess probability (with respect to a Poisson process) of finding two haloes contained in two volume elements $\mathrm{d}V_1$ and $\mathrm{d}V_2$ at a distance r:

$$\mathrm{d}P_{12}(r) \equiv \bar{n}^2[1 + \xi(r)]\mathrm{d}V_1\,\mathrm{d}V_2\,, \tag{11}$$

where $\bar{n}$ is the mean halo (galaxy) number density.

In general, the halo two-point correlation function will depend on the selected halo population ($\mathcal{H}$), the redshift (z) and the cosmological model ($\mathcal{M}$) considered, which we denote as $\xi(r|z, \mathcal{H}, \mathcal{M})$. Because a density perturbation in an expanding universe needs to pass a certain threshold value δ_c[1] in order to be able to collapse and form a gravitationally bound structure (i.e. a halo), the haloes are biased tracers of the underlying smooth matter density field (see e.g. Fry & Gaztanaga 1993). We parametrize this through a simple linear relation:

$$\xi(r|z, \mathcal{H}, \mathcal{M}) = b^2(r|z, \mathcal{H}, \mathcal{M})\xi_{\mathrm{m}}(r|z, \mathcal{M})\,, \tag{12}$$

where $b(r|z, \mathcal{H}, \mathcal{M})$ is the linear bias parameter and $\xi_{\mathrm{m}}(r)$ is the correlation function of the matter density field.

Generally, we can expect that the main differences between ΛCDM and $f(R)$ halo clustering will arise due to (i) different amplitudes of the matter correlation function, ξ_{m}, at the same scale r, and (ii) deviation in the bias parameter, which will be driven by both the departure in the halo mass–bias relation and by the differences in the selection of a particular halo population. We will study the clustering of haloes in redshift space, as this corresponds to what would be available from observations. Therefore, further differences can originate from changes in the effects of redshift-space distortions in different gravity models.

We present in Section 3.1 the method we use to measure the halo correlation function in the simulations. In Section 3.2, we show the halo mass functions obtained in the simulations and we also explain the approach used to select the different halo populations we analyse in Section 4.

[1] The critical density threshold for collapse takes different values in various cosmologies. For ΛCDM, $\delta_c \simeq 1.673$ (Peebles 1980; Weinberg & Kamionkowski 2003). For $f(R)$, this number is no longer universal as the fifth force has an environmental and scale dependence (Li & Efstathiou 2012). Schmidt et al. (2009a) have shown for example that, when the chameleon effect is ignored, the value for F4 is $\delta_c \simeq 1.692$.

3.1 Estimation of the correlation function in the simulations

In this work, we estimate the correlation function for different tracers (haloes or DM particles) extracted from *N*-body simulations. This means that the selection function in all cases is complete, isotropic and homogeneous. Moreover, as the volume is a box with periodic boundary conditions, we do not need to correct for any edge effects. Therefore, we obtain the correlation function in each case using the simple estimator:

$$\hat{\xi}(r) = \frac{DD(r)}{N\bar{n}v(r)} - 1\,, \tag{13}$$

where $DD(r)$ is the number of pairs of tracers with separation in the range $[r, r + \Delta r]$, N is the total number of tracers in the sample, $\bar{n}$ is their number density, and $v(r)$ is the volume of a spherical shell of radius r and width Δr,

$$v(r) = \frac{4\pi}{3}\left[(r + \Delta r)^3 - r^3\right]\,. \tag{14}$$

We use in all cases bins in separation of width $\Delta r = 8\,h^{-1}$ Mpc. This simple estimator is much faster than the estimators usually used for real data, such as that from Landy & Szalay (1993), as in this case we do not need to use an auxiliary random sample to correct for the selection function or edge effects. We checked that we obtained identical results when using the Landy & Szalay (1993) estimator for our calculations.

We compute, for each tracer, the correlation function separately in each of our six realizations and take as our value for the correlation function of this tracer the mean of these six estimations. To estimate the corresponding error, we use the standard error on the mean over the ensemble of six realizations. This is a conservative error estimation (Szapudi & Colombi 1996) that takes into account the contributions of both the cosmic variance and the shot noise. Although cosmic variance is the main source of uncertainty for the DM correlation function, shot noise is also important when we consider samples of massive haloes, with low number density. As we are combining here our six realizations, the statistical error we obtain would correspond to that achievable by an ideal survey covering a volume of $V = 6 \times (1500\,h^{-1}\,\mathrm{Mpc})^3 \simeq 20\,h^{-3}\,\mathrm{Gpc}^3$. When we compute the DM correlation function (in Section 4.1), we use a random subsample containing $\simeq N_p/1000$ DM particles in each realization. This subsample is obtained by randomly selecting particles from the ID list, so that all the population properties are sampled uniformly. This avoids the need for a prohibitive computation time, while not affecting the results, as the errors in the resulting sample are still dominated by cosmic variance, and not by shot noise. For comparison, the resulting number density of DM particles used in our calculations is still $\sim$10 times larger than that of the densest halo sample used (see below).

3.2 Halo mass function and selection of halo populations

Before discussing the halo populations selected for our analysis, we need to consider the halo mass function of our simulations. This is shown for four different times ($z = 0$, 0.25, 0.66, 1.0) in the four panels of Fig. 1. It is quite obvious that our simulations suffer significantly from numerical shot-noise effects at the low-mass end. Due to limited mass and spatial resolution of the simulations, the small-mass haloes suffer from the well-known overmerging effect (Klypin et al. 1999a,b; Moore et al. 1999). Thus, the number density of small-mass haloes is underestimated. This is clearly indicated by the change of slope of the halo mass functions around $M_{200} \sim 2 \times 10^{13}\,h^{-1}\,\mathrm{M}_\odot$. For GR, this mass roughly corresponds to $\bar{n} = 10^{-4}\,h^3\,\mathrm{Mpc}^{-3}$ at $z = 0$, and to $\bar{n} = 3 \times 10^{-5}\,h^3\,\mathrm{Mpc}^{-3}$ at $z = 1$. Although it seems that the magnitude of the resolution effects is very similar in all the models we study (Winther et al. 2015), for the sake of fair comparison we decide to restrict ourselves to this limiting number density as the highest one we consider. As the mass function is always larger for the $f(R)$ models than for GR, this limiting $\bar{n}$ should be sufficient for all our models.

The additional analysis of the plots in Fig. 1 reveals the behaviour already found by other authors (Schmidt et al. 2009a; Hellwing et al. 2013; Li et al. 2013). The largest deviation with respect to the ΛCDM case is observed, as expected, for the F4 model. In this case, the mass function already shows a significant deviation from ΛCDM at $z = 1$, with this deviation slightly increasing towards the largest halo masses. The F5 model, with a more efficient screening, experiences a more complicated behaviour of the halo mass function. Due to the screening, the deviation is very small at the high-mass end, and we observe that the mass at which the halo abundances depart from the fiducial model is growing with time. For both the F4 and F5 models, for the range of halo masses not strongly affected by the screening, the relative departure of the halo number density from the ΛCDM case tends to shrink with time. This reflects the known effect that initially the ΛCDM model experiences a structure formation that is retarded with respect to the MOG models, but at late evolutionary stages the halo growth slows down in the fifth-force cosmologies and so the ΛCDM is able to shrink the initial gap (Hellwing, Juszkiewicz & van de Weygaert 2010). This is mostly due to the relative scarcity of small haloes available for mergers, that is handicapping the halo mass growth via mergers at late times in $f(R)$. Finally, for the F6 model, we do not observe any significant deviation from the ΛCDM case.

We select different halo populations from our simulations by defining a series of *threshold samples*, i.e. selecting haloes with mass above a certain value M_{min}. Since for massive haloes the virial mass–luminosity relation (or mass-to-light ratio) is monotonic and deterministic (Moster et al. 2010), such cuts are equivalent, on a first approximation, to a sample of galaxies selected by luminosity. However, as the virial halo mass is not an observable, a selection with a fixed M_{min} cannot be directly replicated in a real galaxy sample. Instead, we decided to set a fixed number density $\bar{n}(\mathcal{H})$ for each of our samples, and define M_{min} in each model to match it. This approach is in essence a very simple version of the halo abundance matching. As shown in Fig. 1, the halo mass function can be significantly different in $f(R)$ models and in ΛCDM. This means that, for each sample defined in this way, we may end up with significantly different values of M_{min} in each of our models.

We defined three halo populations for the present work, $\mathcal{H}_1, \mathcal{H}_2, \mathcal{H}_3$, with corresponding number densities $\bar{n} = 3 \times 10^{-5}$, 10^{-5} and $3 \times 10^{-6}\,h^3\,\mathrm{Mpc}^{-3}$, respectively. The upper limit for the number density, $\bar{n}(\mathcal{H}_1)$, was chosen based on the resolution limits of the simulations described above. The lower limit $\bar{n}(\mathcal{H}_3)$ was chosen to ensure that shot noise would not dominate our results. These three number densities were used to select the corresponding samples at each of the redshift snapshots used. Table 2 lists the corresponding values of M_{min} used in each case. Following the differences in the mass function shown in Fig. 1, the values are nearly identical for the ΛCDM and F6 models, while they are larger for F5 and F4. As expected, in all cases, for a fixed $\bar{n}$, the corresponding M_{min} increases with decreasing redshift.

The number densities of the selected halo samples can be used to relate them to possible tracers to be used in the analysis of real surveys. The density of $\mathcal{H}_1$, for instance, is similar to that of

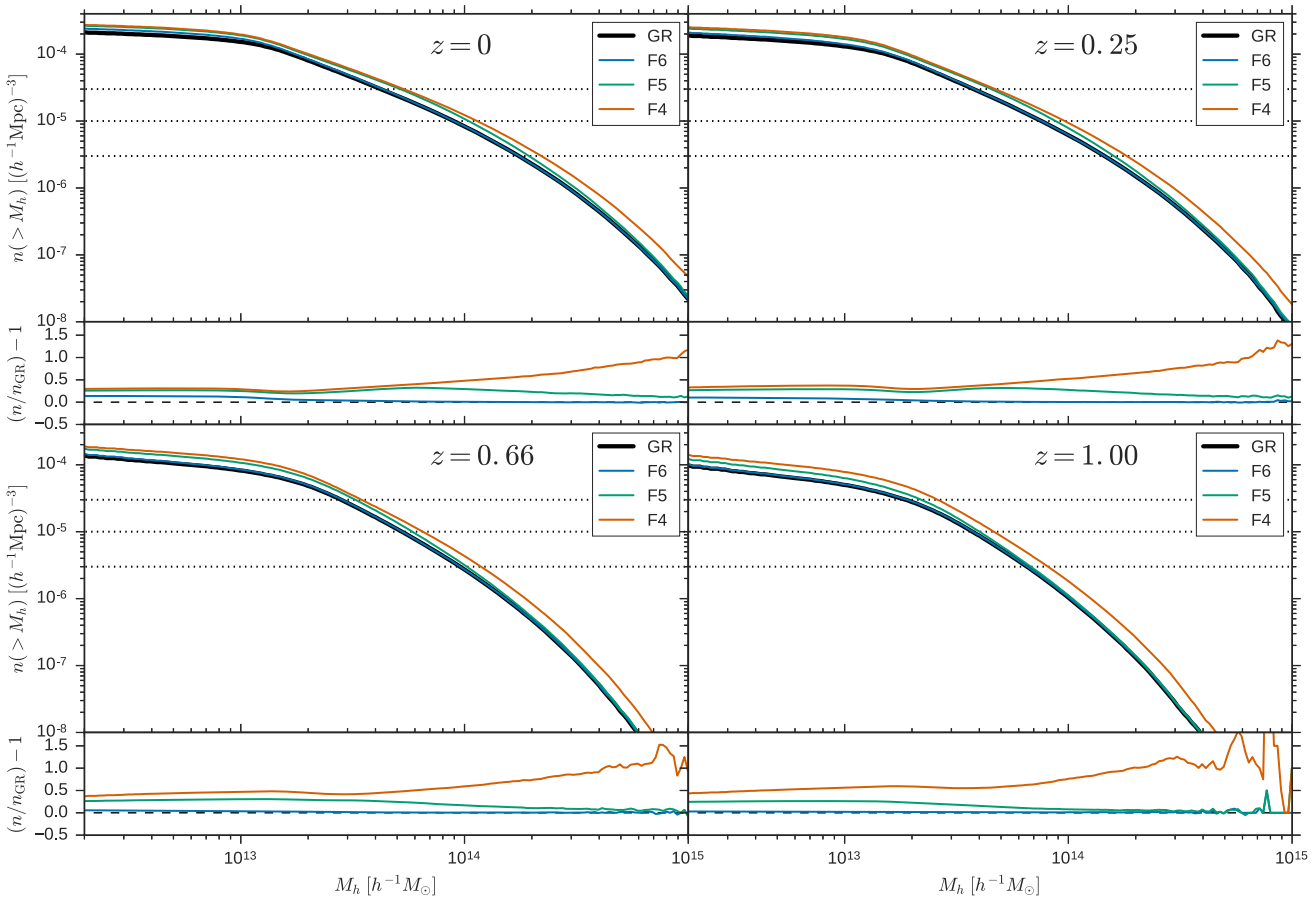

Figure 1. Cumulative halo mass function of the different models considered in this work for the four different epochs $z = 0$, 0.25, 0.66, 1.0, as indicated. The horizontal dotted lines signal the number densities we use to define our three halo samples. In each case, the lower panel shows the relative change with respect to the ΛCDM (GR) model.

Table 2. Properties of the halo samples used in this work. In each case, we list the minimum halo mass M_{min} used to obtain the required number density $\bar{n}$ for a given redshift z.

z	Halo population	$\bar{n}$ (h^3 Mpc^{-3})	M_{min} ($10^{13}\,h^{-1}\,\mathrm{M}_\odot$) GR	F6	F5	F4
0	$\mathcal{H}_1$	3×10^{-5}	4.23	4.31	5.15	5.36
	$\mathcal{H}_2$	10^{-5}	8.94	8.98	10.43	11.39
	$\mathcal{H}_3$	3×10^{-6}	17.50	17.52	19.41	22.07
0.25	$\mathcal{H}_1$	3×10^{-5}	3.77	3.81	4.54	4.71
	$\mathcal{H}_2$	10^{-5}	7.58	7.62	8.77	9.63
	$\mathcal{H}_3$	3×10^{-6}	14.51	14.51	16.02	18.26
0.66	$\mathcal{H}_1$	3×10^{-5}	2.81	2.83	3.25	3.48
	$\mathcal{H}_2$	10^{-5}	5.23	5.26	5.84	6.51
	$\mathcal{H}_3$	3×10^{-6}	9.57	9.59	10.26	11.85
1.00	$\mathcal{H}_1$	3×10^{-5}	1.86	1.91	2.20	2.60
	$\mathcal{H}_2$	10^{-5}	3.73	3.75	4.00	4.65
	$\mathcal{H}_3$	3×10^{-6}	6.53	6.55	6.80	8.10

the brightest samples of luminous red galaxies (LRGs) typically used in the analysis of the Sloan Digital Sky Survey (e.g. Martínez et al. 2009; Kazin et al. 2010). Lower densities as those of $\mathcal{H}_2$, $\mathcal{H}_3$ are typical of galaxy groups or clusters of varying richness (Koester et al. 2007).

4 RESULTS

In this section, we present and discuss our main results obtained for the correlation function of DM and various halo samples at different epochs, both in position and in redshift space. We study the different components affecting the clustering of haloes separately. In Section 4.1, we study the clustering of the underlying matter density field, while in Section 4.2 we analyse the correlation function of haloes, derive the halo bias and assess its properties in the different models.

4.1 Clustering properties of the matter density field

We first study the clustering of the smooth density field of the underlying matter component of our simulations. Although this statistic is not directly accessible via astronomical observations, it is noteworthy to study the properties of ξ_{m}, since it can be related and interpreted in a straightforward manner to the underlying theoretical model. Fig. 2 presents the real-space correlation functions of the DM distributions at the four redshifts considered. In each case, the black line and shaded area correspond to the mean value and 1σ scatter for the ΛCDM model. The corresponding scatter of the MOG runs is of the same order and scale dependence as the fiducial ΛCDM case and hence it is not shown explicitly in the plot for clarity. The different points and colour lines correspond to the three $f(R)$ models considered. The bottom panels in each case show the relative

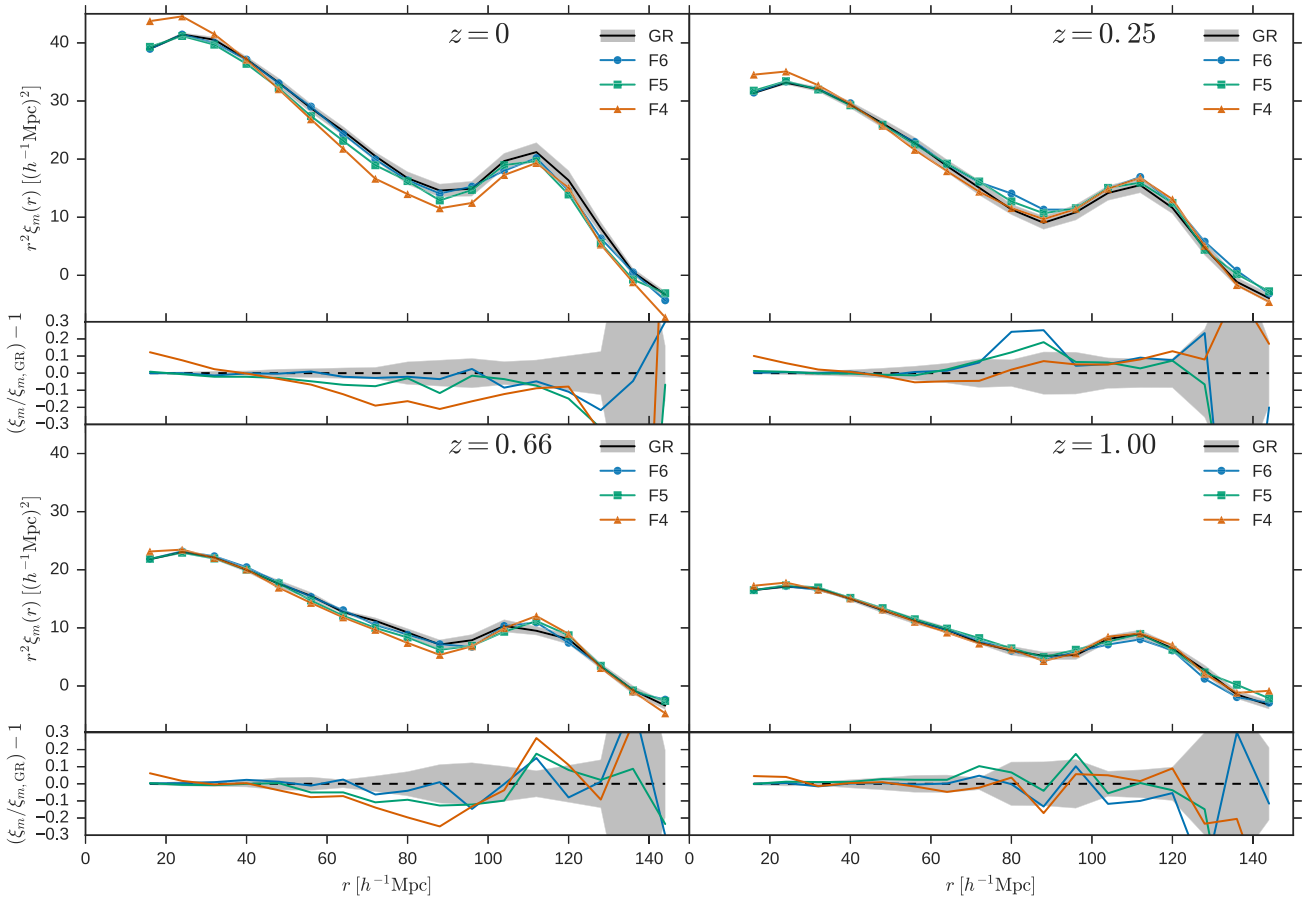

Figure 2. Real-space correlation function of the matter density field, $\xi_{\mathrm{m}}(r)$, for the four models considered. For the GR case, we plot both the mean value (black line) and the 1σ scatter (shaded area) over the six realizations. For the different $f(R)$ models, we only plot the corresponding mean values (colour lines and symbols, as indicated). The corresponding scatter is of the same order and scale dependence as the GR one; hence, we omit it for clarity. We plot the correlation function scaled by r^2 to better visualize the function at large scales, where its amplitude is low. Each plot corresponds to a different epoch, as indicated. In each case, the lower panels show the relative differences with respect to the GR case.

difference of the three $f(R)$ models with respect to the ΛCDM case.

We can already infer a number of interesting points from the data shown in Fig. 2. First, we observe that the amplitude of clustering grows on all scales monotonically with cosmic time. This is a well-known result observed in all classes of cosmologies with hierarchical initial cold dark matter power spectra.

One important feature illustrated by Fig. 2 is the fact that the baryon acoustic oscillations (BAO) peak scale is not affected by MOG. It is apparent from the plot that all models show this peak at a scale $r_{\mathrm{peak}} \simeq 110\,h^{-1}$ Mpc. This corroborates our expectation that the expansion history of the $f(R)$ models is identical to that of ΛCDM when the ratio c_1/c_2 is fixed according to equation (8). However, the position of the peak, and hence the cosmological information that can be extracted from it, could in principle be affected by non-linear effects acting differently in GR and $f(R)$ models. To test this, we did a fit to our results using the simple model commonly used to analyse observations from galaxy redshift surveys (see e.g. Anderson et al. 2014). This model accounts for the non-linear damping of the BAO through the parameter Σ_{NL}, and measures a possible change in the BAO scale with respect to the fiducial value through the parameter α. We find that we recover the correct value of $\alpha = 1$ (and hence of the BAO scale) to within 2 per cent without any significant difference between models. We do not find either any significant difference for Σ_{NL}, with values typically in the range $\Sigma_{\mathrm{NL}} = 7$–$12\,h^{-1}$ Mpc.

While the BAO peak scale is preserved, we can clearly notice in Fig. 2 that all four considered models experience growth of clustering that differ from each other, with differences varying in magnitude and scales at which they appear. At relatively early times, the scalaron fifth force did not have enough time to significantly alter the growth of structures. This is clearly indicated by the results in the bottom-right panel, where at $z = 1$ all models show matter clustering consistent with each other. However, as the cosmic evolution progresses, we can observe a weak change of the correlation function amplitude in the $f(R)$ models.

The F4 model at $z = 0$ manifests a large excess at $r \lesssim 35\,h^{-1}$ Mpc when compared to ΛCDM and the two other $f(R)$ models. This is followed by a lower amplitude of ξ_{m} in the regime from $r \gtrsim 50\,h^{-1}$ Mpc up to the BAO peak. This behaviour reflects the fact that the $f(R)$ models, and especially F4 (which is only very weakly screened), are characterized by a scale-dependent growth rate $f \equiv \mathrm{d}\ln D_+/\mathrm{d}\ln a$ (Koyama et al. 2009). Such a strongly enhanced matter clustering at small scales comes with a price of matter that was more effectively evacuated from the interiors of large cosmic voids (Li et al. 2012b; Cai et al. 2015). The overall effect is very

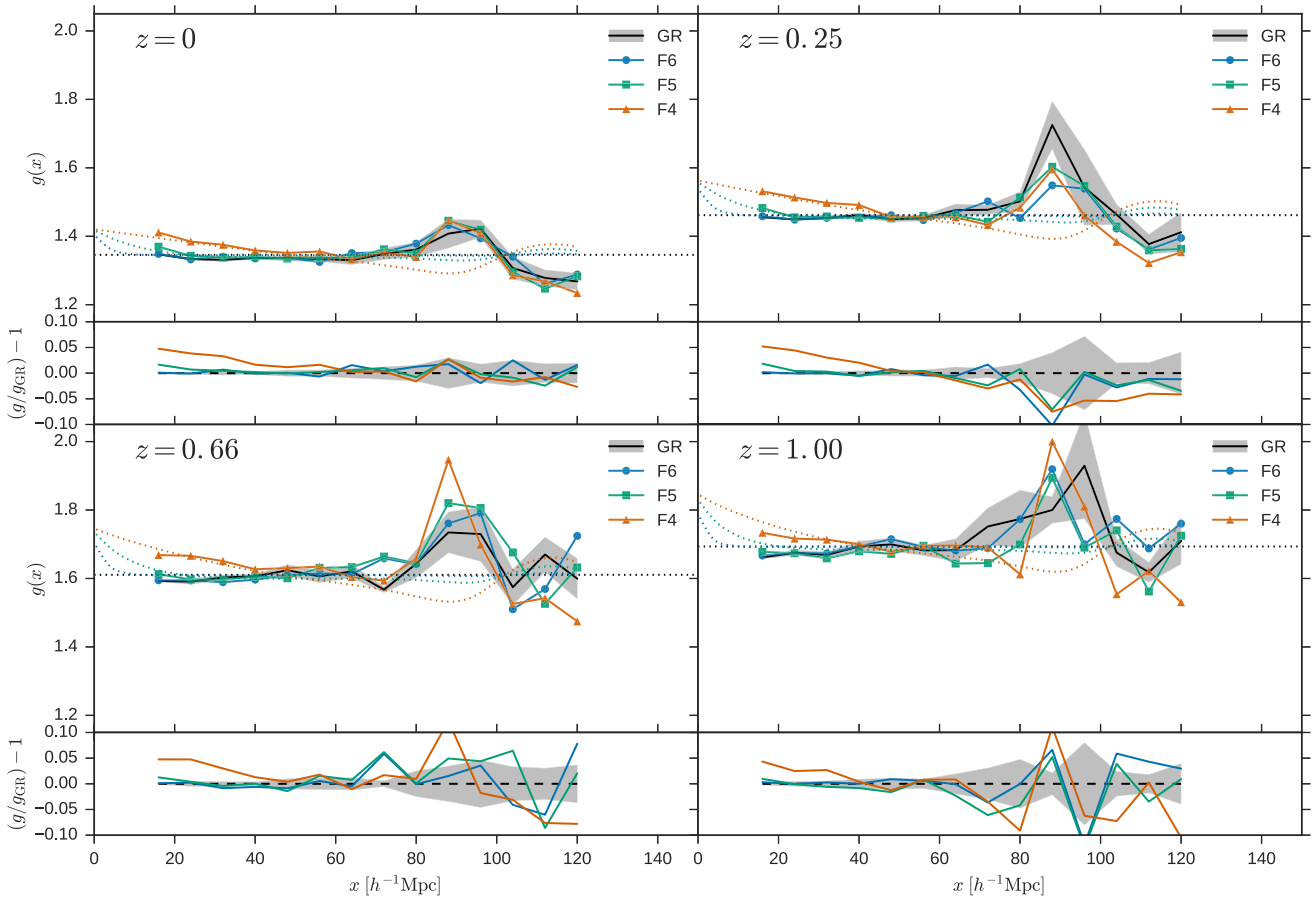

Figure 3. Ratio of the redshift-space to the real-space matter correlation functions, $g(x) = \frac{\xi^s_m(s=x)}{\xi^r_m(r=x)}$. As in previous figures, each plot corresponds to a different epoch, and lower panels show the relative differences with respect to GR. The shaded area corresponds to the 1σ scatter for the GR case. The dotted lines in the main panels illustrate the linear theory prediction $g_L(x)$ for each model. The horizontal black line shows the constant prediction for ΛCDM according to equation (15), while the other lines show the scale-dependent predictions for F6 (blue), F5 (green) and F4 (orange) obtained using equations (16) and (17).

strong in F4, which is indicated by a significantly altered slope of ξ_m at $20 \lesssim r/(h^{-1}\,\mathrm{Mpc}) \lesssim 90$. The F5 model shows a much weaker discrepancy with respect to the GR case. There is a hint of the amplitude of ξ_m being lower than that of ΛCDM at scales of $r \sim 60\,h^{-1}$ Mpc, similar to the F4 case. At smaller scales, however, the F5 model results follow closely those of ΛCDM, as expected from the stronger screening in this case. Similar behaviour (with weaker discrepancies) is found generally for the F4 and F5 models at $z = 0.66$ and 0.25. At $z = 0.25$, we see that the relative amplitudes of the MOG models versus ΛCDM at intermediate scales are slightly larger than expected from the global trends. However, this is a small variation that could be due to a statistical fluctuation. The matter clustering of the F6 model is, at all redshifts, consistent with the ΛCDM case.

To study the effect of redshift-space distortions in the matter density field, we plot in Fig. 3 the ratio of the redshift- to real-space correlation functions $g(x) \equiv \xi^s_m(s = x)/\xi^r_m(r = x)$. The results here can be compared to those of Jennings et al. (2012), who studied the effect of redshift-space distortions in *f*(*R*) cosmologies using power spectrum statistics for the same set of simulations as used in this work.

In each case, we compare our results to the corresponding linear theory predictions. For the ΛCDM model, this corresponds to a constant ratio g, given by the Kaiser formula (Kaiser 1987; Hamilton 1992),

$$g_L^{GR} = 1 + \frac{2}{3}f + \frac{1}{5}f^2\,, \tag{15}$$

where f, the linear growth rate,[2] can be approximated in ΛCDM by $f \approx \Omega_M^{0.55}(z)$. For our cosmogony $g \approx 1.35$ at $z = 0$, growing to $g \approx 1.69$ at $z = 1$. For the case of the *f*(*R*) models, however, the growth rate depends on scale so the predicted ratio does also depend on scale. Koyama et al. (2009) computed the corresponding Fourier-space growth rates for each of our models as a function of wavenumber *f*(*k*). We use these to compute the configuration-space linear prediction $g_L(x)$ for each model as follows. First, from the real-space linear power spectrum $P^r_L(k)$, we obtain the corresponding redshift-space power spectrum $P^s_L(k)$ using the Kaiser formula,

$$P^s_L(k) = \left[1 + \frac{2}{3}f(k) + \frac{1}{5}f(k)^2\right] P^r_L(k)\,. \tag{16}$$

[2] Not to be confused with the non-linear Lagrangian function *f*(*R*).

We use the $P_{\rm L}^{r}(k)$ for each model and redshift obtained by Koyama et al. (2009). We obtain the corresponding real- and redshift-space linear correlation functions using the standard Fourier transform

$$\xi_{\rm L}^{r,s}(x) = 4\pi \int_0^{+\infty} P_{\rm L}^{r,s}(k) \frac{\sin(kx)}{kx} \frac{k^2 {\rm d}k}{(2\pi)^3} , \tag{17}$$

and compute the linear prediction for the $g(x)$ ratio directly as $g_{\rm L}(x) = \xi_{\rm L}^{s}(s = x)/\xi_{\rm L}^{r}(r = x)$. In each panel of Fig. 3, we show as dotted lines the linear theory predictions calculated in this way for GR and our three MOG models.

Fig. 3 illustrates that on scales $x \lesssim 80\,h^{-1}$ Mpc the ratios $g(x)$ for all models follow remarkably well the corresponding linear predictions in each case. This may seem to be in contradiction with the results of Jennings et al. (2012) that showed clearly the damping of the clustering due to virial motions at small scales ($k \gtrsim 0.05\,h\,{\rm Mpc}^{-1}$, see e.g. their fig. 4). However, note that in this work we only consider scales $x \geq 10\,h^{-1}$ Mpc. In the case of ΛCDM, we expect this damping effect to appear only at smaller scales in configuration space (see e.g. Scoccimarro 2004). Our results indicate that this is the case also for the $f(R)$ models.

The results for F5 and F6 in Fig. 3 agree to a good approximation with the measured $g(x)$ for ΛCDM. This is due to the fact that the excess clustering predicted by the scale-dependent growth rates of $f(R)$ appears typically at scales $x \lesssim 20\,h^{-1}$ Mpc for these models – as shown by the linear theory predictions (dotted lines) –, while we study mostly larger scales. In fact, we can observe that F5 deviates from GR at the smallest bin studied, $x = 16\,h^{-1}$ Mpc. F4 is clearly an outlier here, showing a clear enhancement in the ratio $g(x)$ with respect to GR at scales $x \lesssim 50\,h^{-1}$ Mpc. This was to be expected: as we have already mentioned, this model is nearly unscreened; hence, its growth rate is larger than the ΛCDM one over a large range of scales. In the case of F5 and F6, on the other hand, the screening mechanism makes the deviations in the growth factor $f(k)$ with respect to GR to appear only at smaller scales ($k \gtrsim 0.01\,h\,{\rm Mpc}^{-1}$), as shown by fig. 1 of Jennings et al. (2012).

The analysis of the redshift- to real-space matter correlation function ratios also reveals interesting behaviour around the BAO feature. In real space, the BAO feature has the form of a relatively sharp peak in the correlation function centred at the BAO scale (see Fig. 2). In redshift space, the peculiar velocities introduce an smoothing of this BAO feature. This means that the amplitude near the centre of the peak is reduced, and this power is moved to the scales corresponding to the tails of the peak. When plotting the ratio $g(x)$ as in Fig. 3, this results in the observed dip centred at the BAO scale ($x \simeq 110\,h^{-1}$ Mpc), and a peak at slightly smaller scales ($x \simeq 90\,h^{-1}$ Mpc). This behaviour is observed for the four models – GR and $f(R)$ – considered. The apparent larger differences between all models that appear at the peak and dip scales are artificially enhanced due to noise, since we take here a ratio of two very small quantities. In this case, the noise is not expected to be Gaussian, so the simple error estimation we used does not fully account for it.

4.2 Clustering of haloes

Now we turn to analyse the clustering properties of DM haloes. We computed the redshift-space correlation functions $\xi_{\rm h}(s)$ for our three halo populations $\mathcal{H}_1$, $\mathcal{H}_2$ and $\mathcal{H}_3$ described in Section 3.2. We show our results for the four redshifts considered in Fig. 4. Each of the main panels shows the correlation function for the three populations in the four gravity models considered. The lower panels show the relative difference for the three $f(R)$ models with respect to ΛCDM, separately for each halo population. As explained in Section 3, the $\xi_{\rm h}(s)$ we computed correspond to the statistic that can be measured from samples of luminous galaxies or galaxy groups and clusters in real observations. We could therefore compare directly our theoretical results with observational data. Hence, any significant difference we see in Fig. 4 can in principle serve as a way to discriminate between ΛCDM and the $f(R)$ models.

The four panels of Fig. 4 (corresponding to four different redshifts) show the same main property of the clustering of our three halo populations in the four models considered. The least abundant halo samples ($\mathcal{H}_3$) show the highest amplitude of the correlation function, while inversely the highest number density sample ($\mathcal{H}_1$) exhibits the lowest $\xi_{\rm h}(s)$ amplitudes, with the intermediate sample lying in between. This is expected, as higher number density corresponds to lower (average) halo mass (see Table 2) and hence weaker clustering (lower bias parameter).

We focus now on the differences between models observed in the different $\xi_{\rm h}(s)$. For the four considered epochs, the F6 model is very close to the GR data. Hence, the clustering of the three halo populations is statistically indistinguishable in these two models. F4 and F5 show more pronounced differences in all cases. These differences can be appreciated more clearly (especially for F4) for populations $\mathcal{H}_1$ and $\mathcal{H}_2$. This is partly due to the fact that for population $\mathcal{H}_3$ the number of tracers is low; hence, the statistical error is the highest. In general, we observe that the halo correlation functions for these two MOG models are significantly lower than the corresponding ΛCDM ones for scales $s \lesssim 60{-}80\,h^{-1}$ Mpc (or even larger scales in some cases for F4). It is interesting to note the difference in behaviour of the F5 and F4 models. For F5, the departure from the GR signal consists typically of a global change in the amplitude of $\xi_{\rm h}(s)$ for each halo population and redshift. This change in amplitude is visible for redshifts $z \geq 0.25$ but disappears at $z = 0$. In the case of F4, the deviation from GR seems to grow monotonically with time reaching the maximum at $z = 0$. Moreover, in addition to the change in amplitude, we also observe for F4 a change in slope at scales $s \lesssim 60\,h^{-1}$ Mpc with respect to the ΛCDM case. This difference in slope is most clearly visible also at the lowest redshifts $z \leq 0.25$. These differences in the clustering of haloes across redshifts reflect most likely a combination of many different effects: variations in the overall matter clustering (Fig. 2), discrepancies in the magnitude of the redshift-space distortions (Fig. 3) and finally a deviation in halo bias (see equation 12). To infer deeper into this, below we study the halo bias characteristics of our halo populations and the differences between our models.

Following equation (12), we measure the redshift-space halo bias from the simulations using the estimator

$$b_{\rm h}(s) = \sqrt{\frac{\xi_{\rm h}(s)}{\xi_{\rm m}(s)}} . \tag{18}$$

We focus here only on the redshift-space bias as this is the theoretical quantity relevant for comparison with typical observational measurements of ξ in galaxy surveys. However, our results for the real-space bias are very similar to the ones presented here, with only a global change in the amplitude.

Fig. 5 presents the bias as a function of scale s for our three halo populations. We only plot $b(s)$ for $s \leq 110\,h^{-1}$ Mpc to avoid scales where either $\xi_{\rm m}(s)$ or $\xi_{\rm h}(s)$ become negative. As a complementary plot, we also show in Fig. 6 the bias, averaged over a range of scales $s \in [24,\ 52]\,h^{-1}$ Mpc, as a function of the number density of the halo population. We chose these scales as in that range the bias is reliably measured and approximately constant in the case

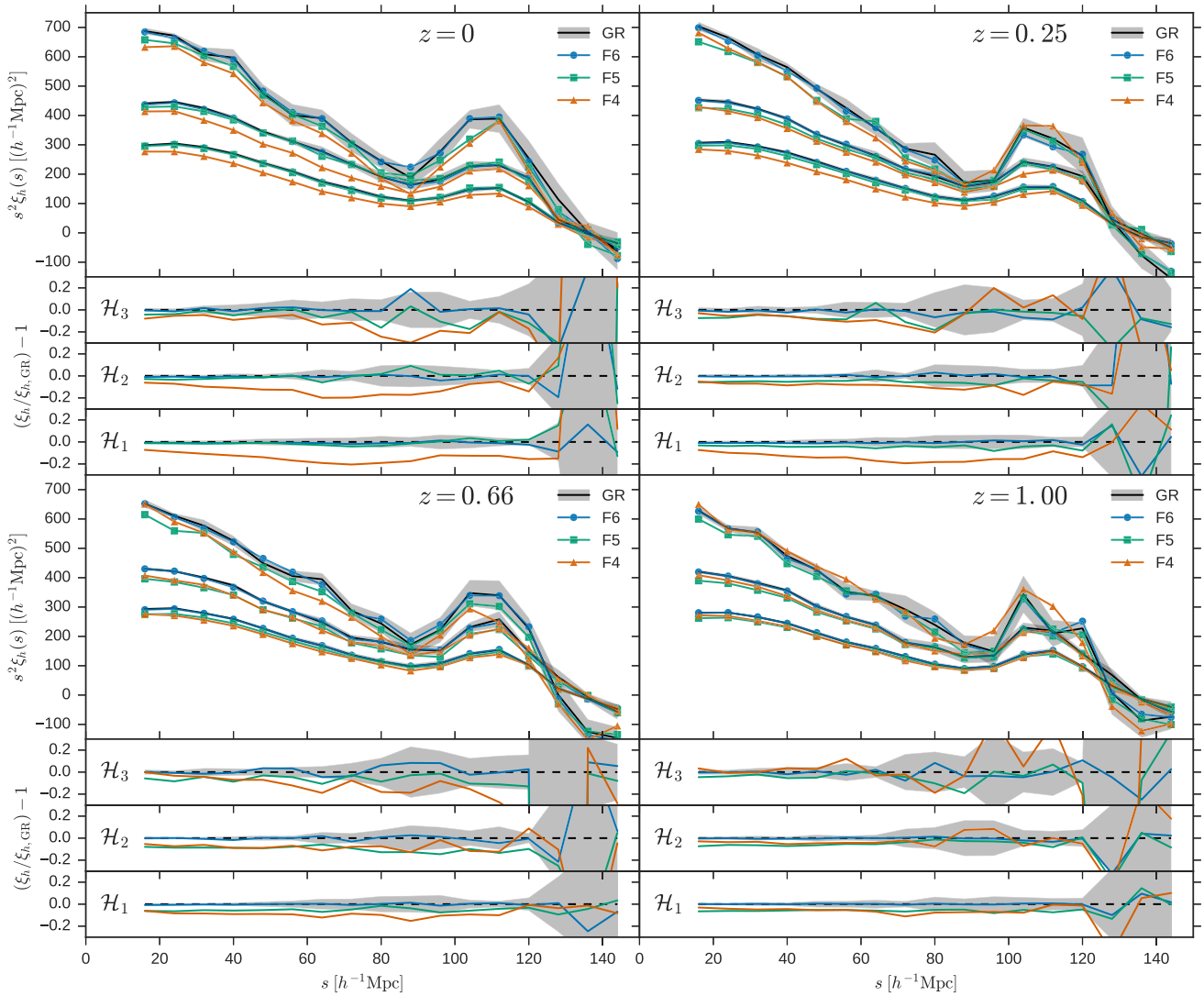

Figure 4. Redshift-space correlation functions of the different halo samples considered, $\xi_{\rm h}(s)$, for our four models. As in Fig. 2, the function amplitudes were rescaled by s^2. As in previous figures, each plot corresponds to a different redshift and the shaded area corresponds to the 1σ scatter for the GR case. In the main panels, the different groups of lines correspond, from bottom to top, to the halo populations $\mathcal{H}_1$, $\mathcal{H}_2$ and $\mathcal{H}_3$. The three lower panels in each plot show the relative differences with respect to GR for the indicated halo population.

of ΛCDM, as shown in Fig. 5. At smaller scales, the non-linear evolution of the density and velocity fields becomes important, and a simple linear bias description breaks down. The rapidly increasing $b(s)$ value observed at $s \lesssim 20\,h^{-1}$ Mpc is a hint of this non-linear behaviour. The weak scale dependence observed at large scales, where $s > 80\,h^{-1}$ Mpc, may also be due to non-linear effects near the BAO peak. However, at these scales, the scatter is large due to cosmic variance and low amplitudes of both matter and halo $\xi(s)$, so these effects are not statistically significant here.

The $f(R)$ halo samples are characterized always by a bias that is either smaller than or equal to the fiducial GR case. If we recall that in $f(R)$ haloes tend to be, on average, more massive than in GR, this result may seem surprising. If we look at a population of haloes at fixed virial mass, in $f(R)$ there will be many haloes that originate from smaller density peaks than their equivalent $z = 0$ mass cousins in GR. Since the initial conditions are the same within the ensemble, haloes that originate from smaller peaks (lower Jeans mass), which are characterized by lower bias, are in $f(R)$ shifted towards higher masses and then compared with the fiducial GR case that originate from rarer peaks (hence higher bias). This is consistent with the picture seen in Fig. 6, where we observe that differences in bias are higher for higher redshift, just as the differences in mass functions in Fig. 1. Another feature of the $f(R)$ halo bias seen in Fig. 5 is its stronger scale dependence than in the ΛCDM case. This can be especially seen for F4, where at $20 \leq s/(\,h^{-1}\,\mathrm{Mpc}) \leq 60$ the bias is increasing with scale. Similar but much weaker behaviour can also be observed for F5 at $z = 0.66$.

Once we have studied the differences in halo bias, we can better interpret the differences in the halo correlation function $\xi_{\rm h}(s)$ observed between the $f(R)$ models F4 and F5 and the ΛCDM case (Fig. 4). For the case of the F4 model, it is clear that the steeper slope and excess clustering at small scales observed for both $\xi_{\rm m}(r)$ (Fig. 2) and $g(x)$ (Fig. 3) are compensated by a significantly smaller bias (and positive scale dependence). This results in the $\xi_{\rm h}(s)$ having in all cases a smaller amplitude than the ΛCDM case, but with only a mild change of slope (except at $z = 0$). A similar explanation can be given for the halo correlation functions in the F5 model, although the differences with respect to ΛCDM in this case are smaller.

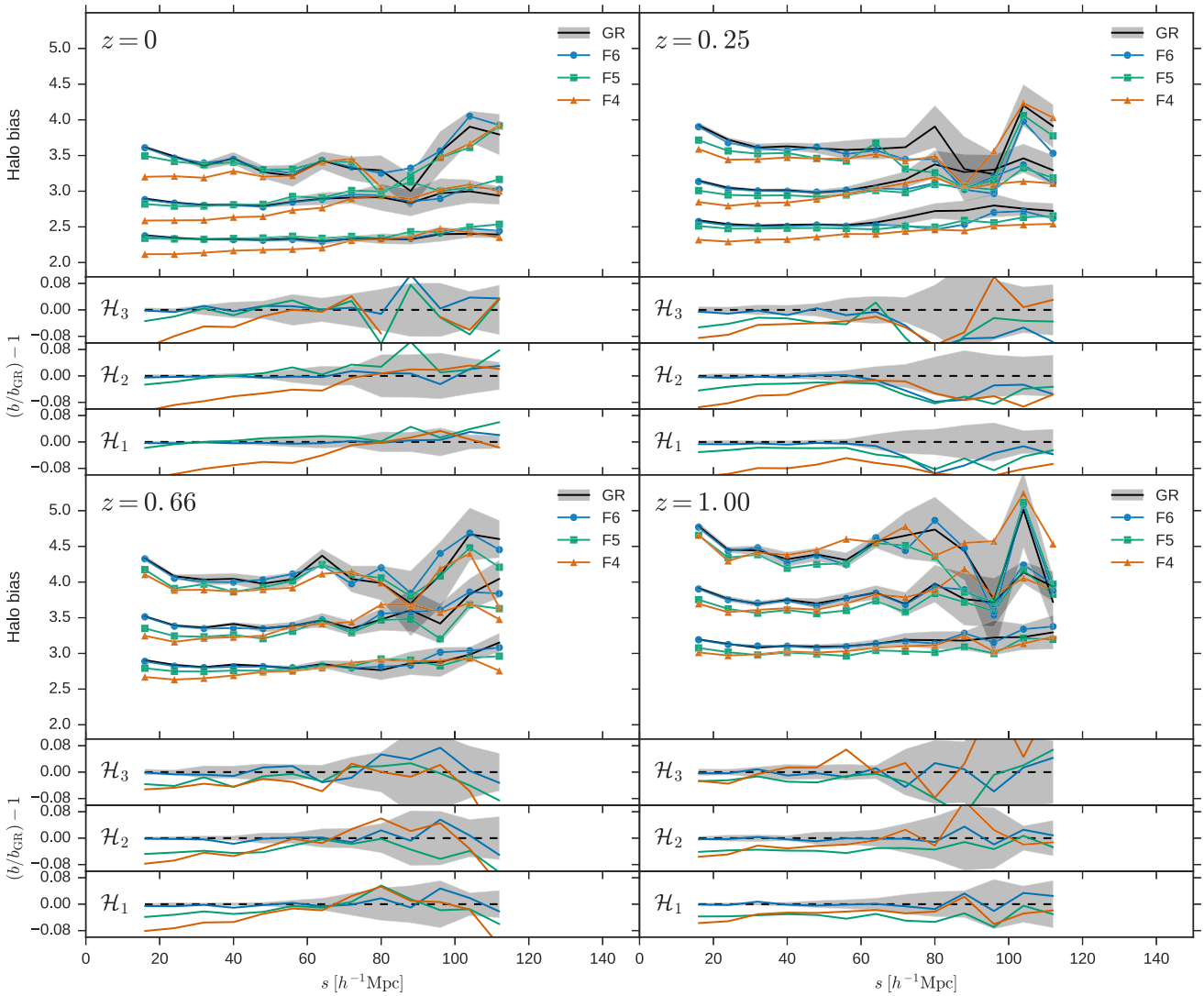

Figure 5. Redshift-space halo bias as a function of scale s for different halo populations. As in previous figures, each plot corresponds to a different redshift and the shaded area corresponds to the 1σ scatter for the GR case. In the main panels, the different groups of lines correspond, from bottom to top, to the bias of halo populations $\mathcal{H}_1$, $\mathcal{H}_2$ and $\mathcal{H}_3$. The three lower panels in each plot show the relative differences with respect to GR for the indicated halo population.

5 OBSERVATIONAL TESTS USING CLUSTERING STATISTICS

The results shown in Section 4.2 indicate that for both F4 and F5 halo samples of the same number density $\bar{n}$ can be characterized typically by significantly different values of the correlation function $\xi_{\rm h}(s)$ than our fiducial GR model. In principle, as our halo samples can be directly related to samples of luminous galaxies or groups in real surveys (with the caveats discussed in Section 3), these $\xi_{\rm h}(s)$ are observable quantities. Hence, they could be used to discriminate between GR and these MOG models. However, the differences in $\xi_{\rm h}(s)$ seen in Fig. 4 could be degenerate with changes in the ΛCDM clustering due to variations of the cosmological parameters, and in particular σ_8. Therefore, one would need to combine the $\xi_{\rm h}(s)$ measurements with other model-independent determinations of these parameters. An alternative would be to measure directly the halo bias and use the differences between models seen in Figs 5 and 6. Bias cannot be directly obtained from two-point statistics, but there exist estimates based on weak lensing observations (McKay et al. 2001; Covone et al. 2014; van Uitert et al. 2016) and on higher order statistics of the galaxy distribution (e.g. Verde et al. 2002; Gaztañaga et al. 2005; McBride et al. 2011; Arnalte-Mur et al. 2016). However, these methods infer bias from observations in a model-dependent way; hence, all the systematic effects were checked only against the assumed ΛCDM cosmology.

In this section, we explore a way in which we can nevertheless use the two-point clustering of haloes to test observationally the studied $f(R)$ models. We try to define a statistic based on the clustering of haloes that (i) can differentiate between ΛCDM and different $f(R)$ models, following our results in Section 4.2, and (ii) can be measured from observations in a way that is as model independent as possible (i.e. does not depend on the clustering properties of the matter density field). As the differences between models observed above vary with both scale and halo population, the best way to define such a statistic is to combine the correlation functions $\xi_{\rm h}(s)$ for different populations and at different scales.

Hence, we define the relative clustering ratio $\mathcal{R}$ for a halo population $\mathcal{H}$ as a function of scale s as

$$\mathcal{R}(s, \mathcal{H}|\mathcal{H}_{\rm ref}, s_{\rm ref}) = \frac{s^2 \xi_{\rm h}(s|\mathcal{H})}{s_{\rm ref}^2 \xi_{\rm h}(s_{\rm ref}|\mathcal{H}_{\rm ref})}\,, \tag{19}$$

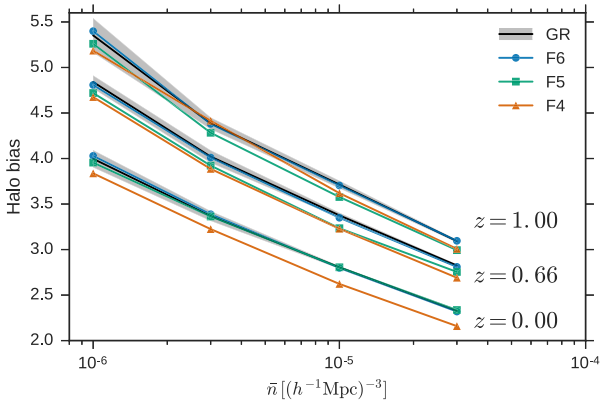

Figure 6. Redshift-space halo bias estimated over the range $s \in [24, 52]\,h^{-1}$ Mpc as a function of the halo density used for selection of the populations. In addition to the samples used elsewhere in this work, we also show for completeness the result for the sample with $\bar{n} = 10^{-6}\,h^3\,\mathrm{Mpc}^{-3}$. The results for three different redshift snapshots, $z = 0$, 0.66 and 1.0, are shown as indicated by the labels. We omit here the results for $z = 0.25$ for clarity.

where $\mathcal{H}_{\rm ref}$ is a reference halo population and $s_{\rm ref}$ is a reference scale (kept fixed). Here we use the term $s^2/s_{\rm ref}^2$ to rescale the correlation functions in order to have comparable values as a function of $s_{\rm ref}$. As we show below, this new statistic can be predicted theoretically for each model using the results of Section 4.2. It can also be directly measured from observations – with the caveats mentioned in Section 3 to identify a halo population with a class of observed objects. The way to compute $\mathcal{R}$ in a given survey is to first identify the relevant populations equivalent to $\mathcal{H}$ and $\mathcal{H}_{\rm ref}$ and obtain the corresponding catalogues of objects. One then computes the redshift-space correlation function for each of these catalogues using a standard estimator (e.g. Landy & Szalay 1993). The clustering ratio $\mathcal{R}$ is finally computed using directly equation (19) above. In this way, $\mathcal{R}$ will be independent of the amplitude of the matter correlation function, σ_8. Furthermore, as both populations $\mathcal{H}$ and $\mathcal{H}_{\rm ref}$ are extracted from the same volume (same survey), the effects of sampling variance of the $\mathcal{R}$ ratio will be additionally suppressed.

Here, we choose for the reference population $\mathcal{H}_{\rm ref} = \mathcal{H}_1$, the sample with the highest spatial abundance, $\bar{n} = 3 \times 10^{-5}\,h^3\,\mathrm{Mpc}^{-3}$. The scale-dependent differences between models in $\xi_{\rm h}(s)$ can appear in different ways in $\mathcal{R}$ depending on the value of $s_{\rm ref}$ used. Therefore, $s_{\rm ref}$ can be chosen, in principle, to maximize the differences between models. Here, we show our results for two reference scales: $s_{\rm ref} = 16$ and $64\,h^{-1}$ Mpc. These two values were chosen to span the range of scales where the discrepancies are more clearly observed in Fig. 4, while avoiding larger scales where errors can grow significantly.

In Figs 7 and 8, we plot the clustering ratio $\mathcal{R}$ for our two reference scales, $s_{\rm ref} = 16$ and $64\,h^{-1}$ Mpc, respectively. The clustering ratio $\mathcal{R}$ for the $\mathcal{H}_1$ population is a special case, as this is the population we use as reference for our calculations. In this case, $\mathcal{R}(s)$ is just the halo correlation function $\xi_{\rm h}(s)$ normalized to its amplitude at $s = s_{\rm ref}$. As the difference between the halo correlation functions of F5 and GR was just a constant shift in the amplitude, this difference completely disappears in the case of $\mathcal{R}$. For the F4 model, however, this difference with respect to GR has a dependence on scale, and therefore we also see a significant deviation in $\mathcal{R}$ at $z = 0$, 0.25 for both values of $s_{\rm ref}$.

When we consider different samples ($\mathcal{H}_2$ and $\mathcal{H}_3$), the situation changes, as here the $\mathcal{R}$ depends also on the relative bias between different populations. For $s_{\rm ref} = 16\,h^{-1}$ Mpc (Fig. 7), F5 presents some departures from GR, exhibiting lower values of $\mathcal{R}$ for $s \lesssim 40\,h^{-1}$ Mpc at $z \leq 0.66$. These departures are small (only a few per cent), but significant for $\mathcal{H}_2$. As these scales (and $s_{\rm ref}$) correspond to the mildly non-linear regime, this could be due to the non-linear effects scaling differently with halo mass in F5 and GR. This discrepancy could be used, in principle, to discriminate between the F5 model and ΛCDM. However, given the small size of the effect, this would be difficult in practice due, e.g. to possible systematic errors.

Moving to the larger reference scale $s_{\rm ref} = 64\,h^{-1}$ Mpc (Fig. 8), the results for F5 are completely consistent with GR. This indicates that the F5 signature at linear scales is reduced to a global change in the amplitude of clustering. On the other side, we obtain here deviations from GR that are large and statistically significant for the least screened $f(R)$ model, F4. These deviations grow with decreasing redshift, attaining relative changes of ∼20 per cent at the smallest scales for all halo populations. For $z \leq 0.25$, the statistical significance of these deviations is $\sim 2\sigma$–5σ. This indicates that $\mathcal{R}(s, \mathcal{H}|\mathcal{H}_1, s_{\rm ref} = 64\,h^{-1}\,\mathrm{Mpc})$ can be used to render constraints for strongly deviating models like F4. As expected from all our previous results, for all the considered snapshots and reference scales, the $\mathcal{R}$ of F6 are statistically consistent with GR.

6 DISCUSSION AND CONCLUSIONS

We have analysed the real- and redshift-space two-point clustering statistics of DM and haloes in a series of simulations employing the structure formation in the ΛCDM and $f(R)$ cosmological models. We have also introduced a new statistic – the halo relative clustering ratios $\mathcal{R}(s, \mathcal{H}|\mathcal{H}_{\rm ref}, s_{\rm ref})$. We have fixed our analysis on three halo populations constructed by implementing fixed number density cuts at $\bar{n} = 3 \times 10^{-5}$, 10^{-5} and $3 \times 10^{-6}\,h^3\,\mathrm{Mpc}^{-3}$ (denoted, respectively, $\mathcal{H}_1$, $\mathcal{H}_2$ and $\mathcal{H}_3$). Hence, our halo populations mimic in a general sense spatial selection effects similar to those found in volume-limited samples from redshift galaxy surveys. The number densities we use are typical of samples of very luminous galaxies, or of groups and clusters of galaxies. We can summarize our most important findings in the following points.

(i) In all models, the clustering amplitude of DM grows monotonically with time. At high redshifts, the matter clustering is indistinguishable among models. At later times ($z \lesssim 0.66$), our strongest model – F4 – shows significant deviations of the amplitude and slope of $\xi_{\rm m}$ at small and intermediate scales, while $\xi_{\rm m}$ of both F5 and F6 remain mostly consistent with ΛCDM. In all models, the BAO peak scale is the same and is not affected in any significant way by the fifth force.

(ii) The ratio, $g(x)$, of redshift- to position-space matter correlation functions of F5 and F6 is compatible at large scales ($x \geq 25\,h^{-1}$ Mpc) with the ΛCDM results. F4 is a strong outlier here, showing significant deviations up to $x \sim 50\,h^{-1}$ Mpc. All four models show good agreement with the respective linear theory predictions in the range $15 \lesssim x/(\,h^{-1}\,\mathrm{Mpc}) \lesssim 80$.

(iii) The differences of the redshift-space two-point correlations of haloes are bigger than in the case of the DM density field. In general, the halo correlation functions of the F4 and F5 models are lower than those of GR. This is more clearly observed for the $\mathcal{H}_1$ and $\mathcal{H}_2$ samples, because of the larger errors in $\mathcal{H}_3$ (due to sparse sampling). The strong F4 model is an outlier at all epochs, with the strongest signal at $z = 0$. However, for the F5 model, the $\xi_{\rm h}$ reaches its maximal departure from GR at intermediate and high redshifts, $z \geq 0.25$.

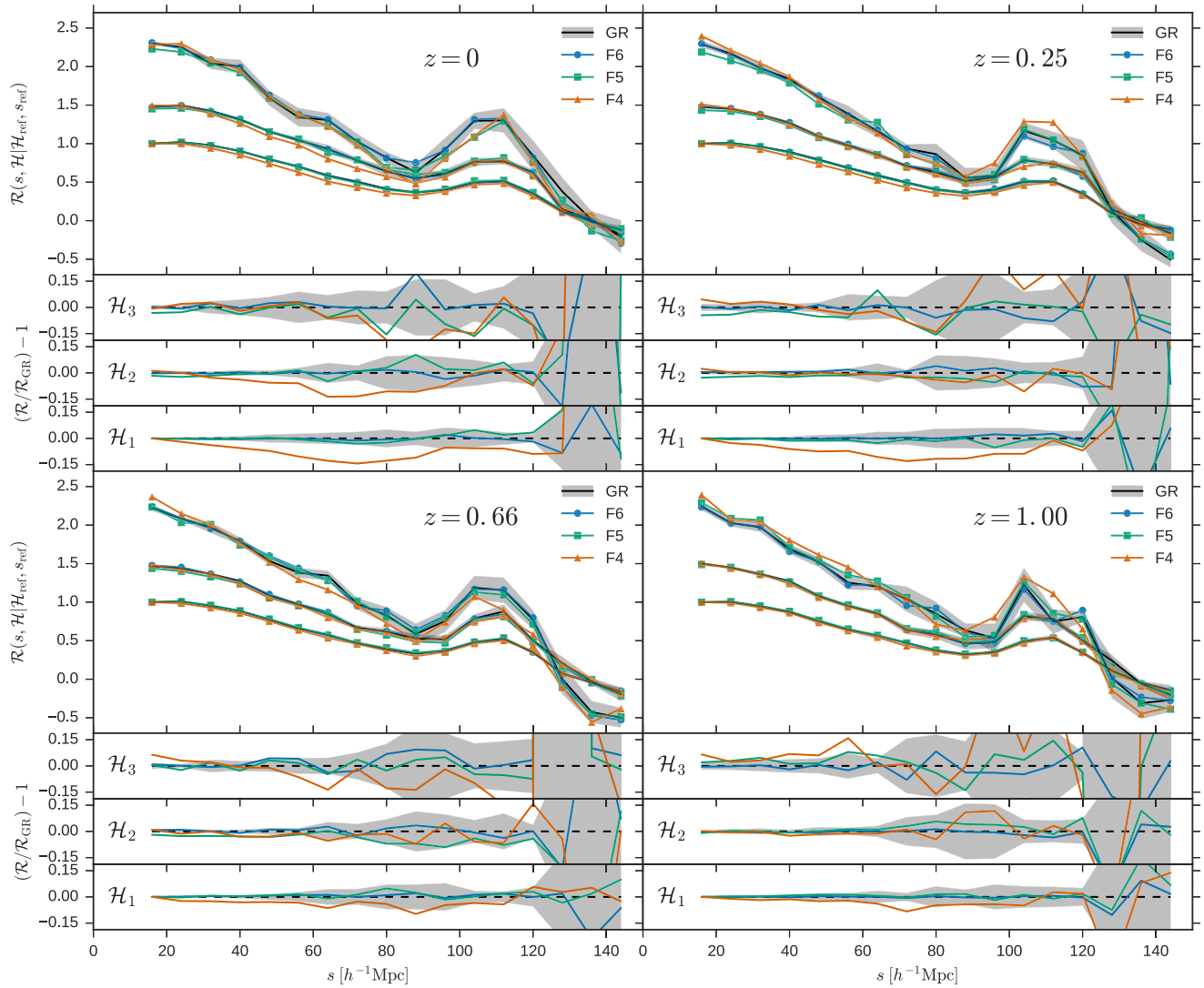

Figure 7. Relative clustering ratio $\mathcal{R}(s, \mathcal{H}|\mathcal{H}_{\rm ref}, s_{\rm ref})$ for different halo populations, for the case in which the reference sample is $\mathcal{H}_{\rm ref} = \mathcal{H}_1$, and the reference scale is set to $s_{\rm ref} = 16\,h^{-1}$ Mpc. As in previous figures, each plot corresponds to a different redshift and the shaded area corresponds to the 1σ scatter for the GR case. In the main panels, the different groups of lines correspond, from bottom to top, to the clustering ratio obtained for halo populations $\mathcal{H}_1$, $\mathcal{H}_2$ and $\mathcal{H}_3$. The three lower panels in each plot show the relative differences with respect to GR for the indicated halo population.

(iv) Halo bias in all $f(R)$ models and for all halo populations is always lower than in GR or consistent with the fiducial model. Again, F4 is an outlier here at all scales and epochs. The F6 model halo bias is fully consistent with the GR predictions, while for F5 the most significant differences appear again at intermediate and high redshifts.

(v) Finally, we considered the relative clustering ratios $\mathcal{R}$ to construct a largely model-independent observational clustering probe. The F4 model halo clustering ratios depart significantly from the GR model for all our samples, especially when using as reference scale $s_{\rm ref} = 64\,h^{-1}$ Mpc and at $z \leq 0.25$. Again, F6 is characterized by too small differences from GR to be statistically distinguishable in any way. However, the $\mathcal{R}$ of the mild F5 model at redshifts of $z \leq 0.66$ and for $s_{\rm ref} = 16\,h^{-1}$ Mpc is showing a small but significant signal at scales $s \lesssim 40\,h^{-1}$ Mpc.

Our results indicate that only in the case of the unrealistically strong and not screened F4 model, one can expect a clear, strong and significant signal visible in both the matter and halo clustering. This signal for F4 is also clear in the clustering ratios $\mathcal{R}$. This means that this model could be tested using only the two-point clustering of haloes in a model-independent way. On the other end of the spectrum, the highly screened F6 model is always very close to GR for all our statistics and samples and at all epochs. Hence, these models are indistinguishable from each other, at least when one is concerned with the two-point clustering statistics. For the physically interesting F5 model, we have found only small differences with respect to GR in the clustering ratios $\mathcal{R}$. It shows, however, a significant signal in the raw halo correlation functions $\xi_{\rm h}(s)$, which can be summarized as changes in a constant linear bias as a function of halo population and redshift (Fig. 6). The predicted signal is strongest for redshifts $z \geq 0.25$. Two-point clustering observations cannot be used to measure the bias on their own. However, our results suggest that they could be used in combination with other probes (e.g. an independent measurement of σ_8) to put constraints on the F5 model.

Our results yield the hope that growing observational data will be able to constrain this class of $f(R)$ models using galaxy clustering.

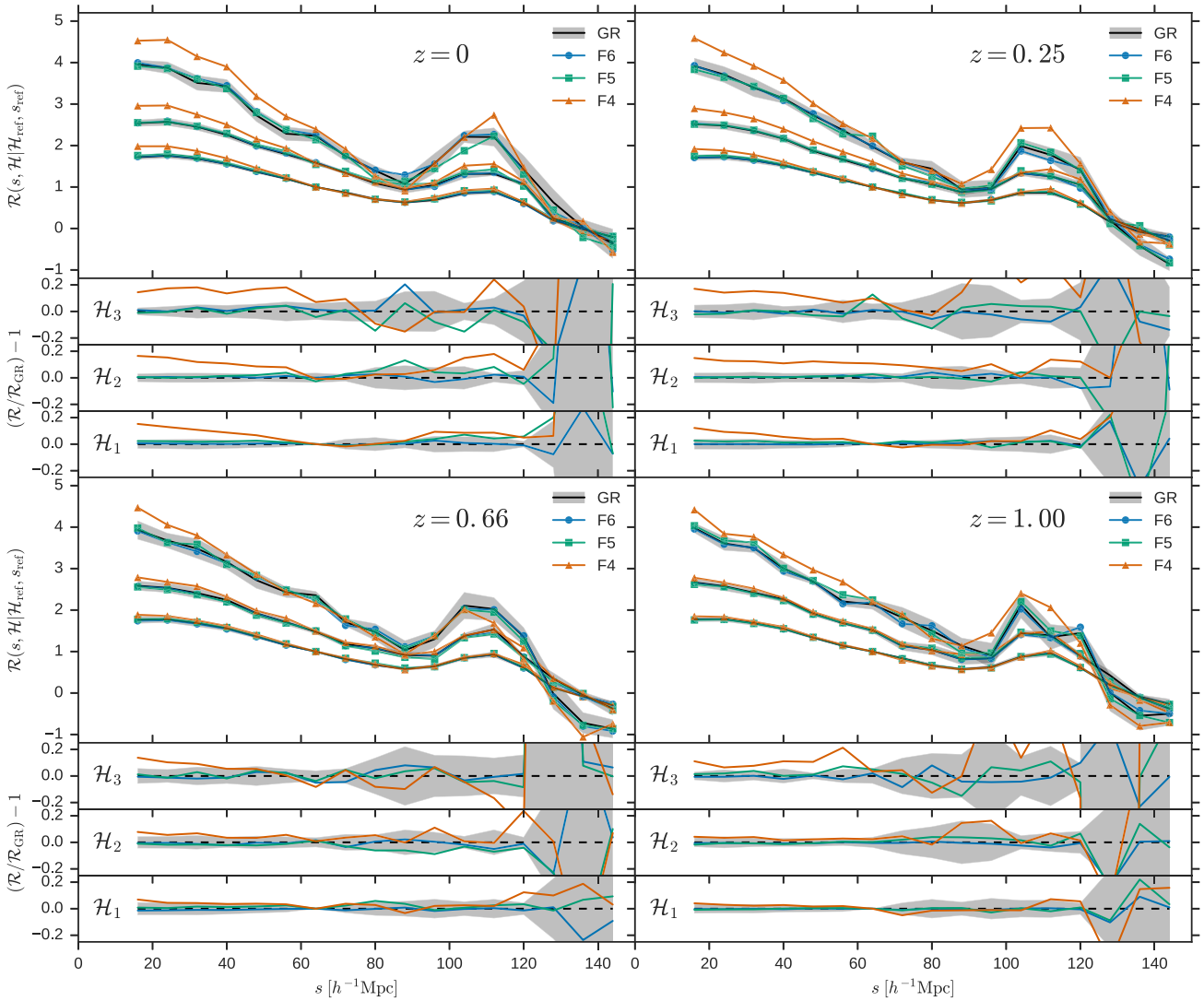

Figure 8. Same as Fig. 7, for the case in which the reference scale is set to $s_{\rm ref} = 64\,h^{-1}$ Mpc.

Two near-term projects that may have the potential to perform these tests are the DESI (Levi et al. 2013; DESI Collaboration et al. 2016) and J-PAS (Benitez et al. 2014) surveys, which will cover a large fraction of the sky (14 000 deg^2 and 8500 deg^2, respectively). Both projects will target different classes of galaxies up to redshifts $z \lesssim 1$, therefore covering the range of redshifts studied in this work. Given the expected number density, it will be possible to select samples of galaxies (e.g. LRGs) that can be related to the halo populations we studied. It will also be possible to use for these tests catalogues of galaxy groups and clusters from these surveys. Ascaso et al. (2016) showed that it will be possible to detect reliably in J-PAS clusters corresponding to halo masses of $M \gtrsim 3.6 \times 10^{13}\,h^{-1}\,{\rm M}_\odot$ up to $z \simeq 0.7$ (assuming a ΛCDM cosmology). This selection would match our $\mathcal{H}_1$ sample at the lowest redshifts. Slightly further in the future, another survey suitable for this type of analysis will be *Euclid* (Laureijs et al. 2011). *Euclid* will observe galaxies over a significantly larger volume, thus reducing the statistical error of the clustering measurements. However, its spectroscopic survey will be limited to higher redshifts than those studied in this work ($z \gtrsim 0.9$), where we expect the differences in clustering between the GR and *f*(*R*) to be smaller.

We therefore expect that our method will be able to constrain the particular Hu & Sawicki (2007) model considered here down to $|f_{R0}| \simeq 10^{-5}$ using data from these near-future surveys. This is competitive with possible constraints using other known methods. DESI Collaboration et al. (2016), for example, forecast that in the ideal case DESI will be able to measure the growth rate f at scales $k \leq 0.1\,h\,{\rm Mpc}^{-1}$ to a precision of $\simeq$ 2–4 per cent for redshifts $z \in [0.6, 1.0]$ (see their tables 2.3 and 2.4). For comparison, Jennings et al. (2012) show that the maximum expected change in f with respect to GR at these scales and redshifts is $\simeq 5$ per cent ($\simeq 1$ per cent) for $|f_{R0}| \sim 10^{-5}$ ($|f_{R0}| \sim 10^{-6}$). Therefore, this type of measurements could yield constraints of the same order as those achievable using the clustering ratios $\mathcal{R}$. Alternatively, Cataneo et al. (2015) predict that it will be possible to obtain even better constraints when future surveys allow for the detailed measurement of the cluster and group mass function to higher redshifts ($z \sim 2$).

Our analysis of the $g(x) \equiv \xi^s_{\rm m}(x)/\xi^r_{\rm m}(x)$ ratios showed, however, that one needs to take caution when trying to extract the growth rate f from just the halo/galaxy/matter clustering signal. Although the scale-dependent growth rates predict an enhancement in the redshift-space clustering in *f*(*R*) models, this is only seen at relatively

small scales, $x < 20\,h^{-1}$ Mpc ($x < 50\,h^{-1}$ Mpc in F4). At these small scales, we will find deviations from linear theory due to the effect of virial motions, and one should take into account the predicted enhanced peculiar velocities in MOG models (Hellwing et al. 2014; Zu et al. 2014; Sabiu et al. 2016). That means that, in order to use the growth rate inferred from galaxy redshift catalogues to constrain this class of models, it is necessary to model these effects in detail, and to test the analysis method with realistic MOG mocks (Barreira, Sánchez & Schmidt 2016). This problem is largely alleviated in the case where we only consider redshift-space related quantities, such as the halo correlation function $\xi_{\rm h}(s)$ or especially the clustering ratios $\mathcal{R}$, and so avoid the necessity of modelling precisely the connection between position- and redshift-space objects. In sum, we advertise here to use $\mathcal{R}(s, \mathcal{H}|\mathcal{H}_{\rm ref}, s_{\rm ref})$ to study and constrain $f(R)$ models using the redshift-space clustering of galaxies as measured by modern galaxy surveys.

ACKNOWLEDGEMENTS

We thank the referee, Dr Nelson Lima, for his comments that helped improve the clarity of the paper. We are very grateful to Baojiu Li for many inspiring comments and for providing cosmological simulations used in this work. We have also benefited from comments and discussions we had with Shaun Cole, Carlos Frenk, Kazuya Koyama, Will Percival and Violeta González-Pérez. WAH is grateful to the co-authors for the endless patience they showed during writing of this draft. PAM was supported by the European Research Council Starting Grant (DEGAS-259586) and by the Generalitat Valenciana project PrometeoII 2014/060, and acknowledges additional support from the Spanish Ministry for Economy and Competitiveness through grants AYA2013-48623-C2-2 and AYA2016-81065-C2-2-P. WAH acknowledges support from the European Research Council grant through 646702 (CosTesGrav) and the Polish National Science Center under contract #UMO-2012/07/D/ST9/02785. PN acknowledges the support of the Royal Society through the award of a University Research Fellowship, the European Research Council, through receipt of a Starting Grant (DEGAS-259586) and the Science and Technology Facilities Council (ST/L00075X/1). This work used the DiRAC Data Centric system at Durham University, operated by the Institute for Computational Cosmology on behalf of the STFC DiRAC HPC Facility (www.dirac.ac.uk). This equipment was funded by BIS National E-infrastructure capital grant ST/K00042X/1, STFC capital grant ST/H008519/1, and STFC DiRAC Operations grant ST/K003267/1 and Durham University. DiRAC is part of the National E-Infrastructure. This research was carried out with the support of the HPC Infrastructure for Grand Challenges of Science and Engineering Project, co-financed by the European Regional Development Fund under the Innovative Economy Operational Programme. This research made use of MATPLOTLIB, a PYTHON library for publication quality graphics (Hunter 2007).

REFERENCES

Abbott B. P. et al., 2016, Phys. Rev. Lett., 116, 061102
Alam S. et al., 2016, MNRAS, preprint (arXiv:1607.03155)
Allen S. W., Evrard A. E., Mantz A. B., 2011, ARA&A, 49, 409
Anderson L. et al., 2014, MNRAS, 441, 24
Arnalte-Mur P., Vielva P., Martínez V. J., Sanz J. L., Saar E., Paredes S., 2016, J. Cosmol. Astropart. Phys., 3, 005
Ascaso B. et al., 2015, MNRAS, 452, 549
Ascaso B. et al., 2016, MNRAS, 456, 4291
Barreira A., Sánchez A. G., Schmidt F., 2016, Phys. Rev. D, 94, 084022
Bartelmann M., Schneider P., 2001, Phys. Rep., 340, 291
Baugh C. M., 2006, Rep. Prog. Phys., 69, 3101
Behroozi P. S., Wechsler R. H., Wu H.-Y., 2013, ApJ, 762, 109
Benitez N. et al., 2014, preprint (arXiv:1403.5237)
Berry C. P. L., Gair J. R., 2011, Phys. Rev. D, 83, 104022
Berti E. et al., 2015, Class. Quantum Grav., 32, 243001
Bose S., Hellwing W. A., Li B., 2015, J. Cosmol. Astropart. Phys., 2, 034
Bose S., Li B., Barreira A., He J.-h., Hellwing W. A., Koyama K., Llinares C., Zhao G.-B., 2016, preprint (arXiv:1611.09375)
Brax P., van de Bruck C., Davis A.-C., Shaw D. J., 2008, Phys. Rev. D, 78, 104021
Brax P., Davis A.-C., Li B., Winther H. A., 2012, Phys. Rev. D, 86, 044015
Brax P., Davis A. C., Sakstein J., 2014, Class. Quantum Grav., 31, 225001
Cai Y.-C., Padilla N., Li B., 2015, MNRAS, 451, 1036
Carroll S. M., 2001, Living Rev. Relativ., 4, 1
Carroll S. M., De Felice A., Duvvuri V., Easson D. A., Trodden M., Turner M. S., 2005, Phys. Rev. D, 71, 063513
Cataneo M. et al., 2015, Phys. Rev. D, 92, 044009
Chiba T., Smith T. L., Erickcek A. L., 2007, Phys. Rev. D, 75, 124014
Clifton T., Ferreira P. G., Padilla A., Skordis C., 2012, Phys. Rep., 513, 1
Cole S. et al., 2005, MNRAS, 362, 505
Colombi S., Bouchet F. R., Schaeffer R., 1994, A&A, 281, 301
Contreras S., Baugh C. M., Norberg P., Padilla N., 2013, MNRAS, 432, 2717
Copeland E. J., Sami M., Tsujikawa S., 2006, Int. J. Mod. Phys. D, 15, 1753
Covone G., Sereno M., Kilbinger M., Cardone V. F., 2014, ApJ, 784, L25
de Felice A., Tsujikawa S., 2010, Living Rev. Relativ., 13, 3
DESI Collaboration et al., 2016, preprint (arXiv:1611.00036)
Eisenstein D. J. et al., 2005, ApJ, 633, 560
Fabjan D., Borgani S., Tornatore L., Saro A., Murante G., Dolag K., 2010, MNRAS, 401, 1670
Faulkner T., Tegmark M., Bunn E. F., Mao Y., 2007, Phys. Rev. D, 76, 063505
Ferraro S., Schmidt F., Hu W., 2011, Phys. Rev. D, 83, 063503
Fontanot F., Puchwein E., Springel V., Bianchi D., 2013, MNRAS, 436, 2672
Fry J. N., Gaztanaga E., 1993, ApJ, 413, 447
Gaztañaga E., Norberg P., Baugh C. M., Croton D. J., 2005, MNRAS, 364, 620
Gil-Marín H., Schmidt F., Hu W., Jimenez R., Verde L., 2011, J. Cosmol. Astropart. Phys., 11, 19
Guo Q., Cooper A. P., Frenk C., Helly J., Hellwing W. A., 2015, MNRAS, 454, 550
Hamilton A. J. S., 1992, ApJ, 385, L5
Harnois-Déraps J., Munshi D., Valageas P., van Waerbeke L., Brax P., Coles P., Rizzo L., 2015, MNRAS, 454, 2722
He J.-h., Li B., Baugh C. M., 2016, Phys. Rev. Lett., 117, 221101
Hellwing W., 2015, in Biernacka M., Bajan K., Stachowski G., Flin P., eds, Proc. of the Polish Astron. Soc. Vol. 2, Introduction to Cosmology. Polish Astron. Soc., Warsaw, p. 58
Hellwing W. A., Juszkiewicz R., van de Weygaert R., 2010, Phys. Rev. D, 82, 103536
Hellwing W. A., Li B., Frenk C. S., Cole S., 2013, MNRAS, 435, 2806
Hellwing W. A., Barreira A., Frenk C. S., Li B., Cole S., 2014, Phys. Rev. Lett., 112, 221102
Hellwing W. A., Schaller M., Frenk C. S., Theuns T., Schaye J., Bower R. G., Crain R. A., 2016, MNRAS, 461, L11
Hinshaw G. et al., 2013, ApJS, 208, 19
Hu W., Sawicki I., 2007, Phys. Rev. D, 76, 064004
Hunter J. D., 2007, Comput. Sci. Eng., 9, 90
Jackson J. C., 1972, MNRAS, 156, 1p
Jennings E., Baugh C. M., Li B., Zhao G.-B., Koyama K., 2012, MNRAS, 425, 2128
Kaiser N., 1987, MNRAS, 227, 1
Kazin E. A. et al., 2010, ApJ, 710, 1444
Khoury J., Weltman A., 2004, Phys. Rev. D, 69, 044026

Klypin A., Gottlöber S., Kravtsov A. V., Khokhlov A. M., 1999a, ApJ, 516, 530
Klypin A., Kravtsov A. V., Valenzuela O., Prada F., 1999b, ApJ, 522, 82
Knebe A. et al., 2011, MNRAS, 415, 2293
Koester B. P. et al., 2007, ApJ, 660, 239
Koyama K., 2016, Rep. Prog. Phys., 79, 046902
Koyama K., Taruya A., Hiramatsu T., 2009, Phys. Rev. D, 79, 123512
Kravtsov A. V., Berlind A. A., Wechsler R. H., Klypin A. A., Gottlöber S., Allgood B., Primack J. R., 2004, ApJ, 609, 35
Landy S. D., Szalay A. S., 1993, ApJ, 412, 64
Laureijs R. et al., 2011, preprint (arXiv:1110.3193)
Levi M. et al., 2013, preprint (arXiv:1308.0847)
Li B., Efstathiou G., 2012, MNRAS, 421, 1431
Li B., Zhao G.-B., Teyssier R., Koyama K., 2012a, J. Cosmol. Astropart. Phys., 1, 51
Li B., Zhao G.-B., Koyama K., 2012b, MNRAS, 421, 3481
Li B., Hellwing W. A., Koyama K., Zhao G.-B., Jennings E., Baugh C. M., 2013, MNRAS, 428, 743
Li B., He J.-h., Gao L., 2016, MNRAS, 456, 146
Liu X. et al., 2016, Phys. Rev. Lett., 117, 051101
Llinares C., Mota D. F., 2013, Phys. Rev. Lett., 110, 161101
Llinares C., Mota D. F., 2014, Phys. Rev. D, 89, 084023
Llinares C., Knebe A., Zhao H., 2008, MNRAS, 391, 1778
Lombriser L., Slosar A., Seljak U., Hu W., 2012, Phys. Rev. D, 85, 124038
McBride C. K., Connolly A. J., Gardner J. P., Scranton R., Scoccimarro R., Berlind A. A., Marín F., Schneider D. P., 2011, ApJ, 739, 85
McCarthy I. G. et al., 2010, MNRAS, 406, 822
McCarthy I. G., Schaye J., Bower R. G., Ponman T. J., Booth C. M., Dalla Vecchia C., Springel V., 2011, MNRAS, 412, 1965
McKay T. A. et al., 2001, ApJ, preprint (astro-ph/0108013)
Mandelbaum R., Seljak U., Kauffmann G., Hirata C. M., Brinkmann J., 2006, MNRAS, 368, 715
Martínez V. J., Arnalte-Mur P., Saar E., de la Cruz P., Pons-Bordería M. J., Paredes S., Fernández-Soto A., Tempel E., 2009, ApJ, 696, L93
Moore B., Ghigna S., Governato F., Lake G., Quinn T., Stadel J., Tozzi P., 1999, ApJ, 524, L19
Moster B. P., Somerville R. S., Maulbetsch C., van den Bosch F. C., Macciò A. V., Naab T., Oser L., 2010, ApJ, 710, 903
Navarro I., Van Acoleyen K., 2007, J. Cosmol. Astropart. Phys., 2, 22
Oyaizu H., 2008, Phys. Rev. D, 78, 123523
Oyaizu H., Lima M., Hu W., 2008, Phys. Rev. D, 78, 123524
Peebles P. J. E., 1980, The large-Scale Structure of the Universe. Princeton Univ. Press, Princeton, NJ
Perlmutter S. et al., 1999, ApJ, 517, 565
Planck Collaboration XIII, 2016, A&A, 594, A13
Puchwein E., Springel V., 2013, MNRAS, 428, 2966
Puchwein E., Baldi M., Springel V., 2013, MNRAS, 436, 348
Raveri M., Baccigalupi C., Silvestri A., Zhou S.-Y., 2015, Phys. Rev. D, 91, 061501
Reid B. A., Spergel D. N., Bode P., 2009, ApJ, 702, 249
Riess A. G. et al., 1998, AJ, 116, 1009
Robotham A. S. G. et al., 2011, MNRAS, 416, 2640
Sabiu C. G., Mota D. F., Llinares C., Park C., 2016, A&A, 592, A38
Sakstein J., 2013, Phys. Rev. D, 88, 124013
Sakstein J., 2015, Phys. Rev. D, 92, 124045
Schaye J. et al., 2010, MNRAS, 402, 1536
Schaye J. et al., 2015, MNRAS, 446, 521
Schmidt F., Lima M., Oyaizu H., Hu W., 2009a, Phys. Rev. D, 79, 083518
Schmidt F., Vikhlinin A., Hu W., 2009b, Phys. Rev. D, 80, 083505
Schrabback T. et al., 2010, A&A, 516, A63
Scoccimarro R., 2004, Phys. Rev. D, 70, 083007
Sotiriou T. P., Faraoni V., 2010, Rev. Mod. Phys., 82, 451
Spergel D. N. et al., 2007, ApJS, 170, 377
Suyu S. H. et al., 2013, ApJ, 766, 70
Szapudi I., Colombi S., 1996, ApJ, 470, 131
Umetsu K., Zitrin A., Gruen D., Merten J., Donahue M., Postman M., 2016, ApJ, 821, 116
van Daalen M. P., Schaye J., Booth C. M., Dalla Vecchia C., 2011, MNRAS, 415, 3649
van Daalen M. P., Schaye J., McCarthy I. G., Booth C. M., Dalla Vecchia C., 2014, MNRAS, 440, 2997
van Uitert E., Gilbank D. G., Hoekstra H., Semboloni E., Gladders M. D., Yee H. K. C., 2016, A&A, 586, A43
Verde L. et al., 2002, MNRAS, 335, 432
Vogelsberger M. et al., 2014, MNRAS, 444, 1518
Weinberg N. N., Kamionkowski M., 2003, MNRAS, 341, 251
Wilcox H., Nichol R. C., Zhao G.-B., Bacon D., Koyama K., Romer A. K., 2016, MNRAS, 462, 715
Will C. M., 2014, Living Rev. Relativ., 17, 4
Winther H. A. et al., 2015, MNRAS, 454, 4208
Wojtak R., Hansen S. H., Hjorth J., 2011, Nature, 477, 567
Zehavi I. et al., 2011, ApJ, 736, 59
Zhao G.-B., Li B., Koyama K., 2011, Phys. Rev. D, 83, 044007
Zheng Z., Zehavi I., Eisenstein D. J., Weinberg D. H., Jing Y. P., 2009, ApJ, 707, 554
Zu Y., Weinberg D. H., Jennings E., Li B., Wyman M., 2014, MNRAS, 445, 1885

This paper has been typeset from a TEX/LATEX file prepared by the author.